SEG Special Publications, no. 24, pp. 101–120

Chapter 7

Magmatic Sulfides from the Rincón-Portezuelo de las Ánimas Volcanic Complex, Northwest Argentina: Insights on Magma Fertility and Comparison with Mineralized Volcanic Systems

A. Gioncada,[1] P. Fulignati,[1,†] L.Vezzoli,[2] R. Omarini,[3,*] D. Bosch,[4] O. Bruguier,[4] R. Mazzuoli,[1] and V. Lopez-Azarevich[3]

[1]*Dipartimento di Scienze della Terra, University of Pisa, Via S. Maria 53, 56126 Pisa, Italy*

[2]*CNR-IGG, Institute of Geosciences and Earth Resources, Via G. Moruzzi 1, 56124 Pisa, Italy*

[3]*Facultad de Ciencias Naturales, Universidad Nacional de Salta, CEGA-CONICET Salta, Argentina*

[4]*Géosciences Montpellier, Université de Montpellier, CNRS, Université des Antilles, Montpellier, France*

Abstract

The composition and fate of magmatic sulfides are some of the most critical factors invoked to play a role in the chalcophile metal fertility of arc magmas. Examination of magmatic sulfide accessory minerals in nonmineralized volcanic systems may help to understand the behavior of chalcophile metals at sulfide saturation. This study presents compositional data on magmatic sulfides in lavas of the late Miocene Rincón-Portezuelo de las Ánimas Volcanic Complex, northwest Argentina. This is the easternmost magmatic occurrence in the back arc of the Southern Central Andes, at 27°S, about 75 km northeast from the world-class Bajo de la Alumbrera porphyry Cu-Au deposit. At this latitude the late Miocene volcanic activity migrated eastward as a consequence of the shallowing slab subduction. Both copper-rich and pyrrhotite magmatic sulfide inclusions have been identified in the Rincón-Portezuelo de las Ánimas volcanic suite, straddling the high K calc-alkaline–shoshonite boundary. We discuss the sulfide composition in the framework of magmatic evolution and in comparison to the metal content of magmatic sulfides of the coeval Farallón Negro Volcanic Complex, associated with the Bajo de la Alumbrera porphyry Cu-Au and other mineralized systems. The results show that sulfide liquid, exsolved from silicate melts of intermediate composition, stores Cu, Pb, Ag, and Bi in crystal mushes, reducing the mineralizing potential of residual melts while fertilizing the middle-upper crust. Gold behavior seems to be controlled by additional mechanisms, linked to the magma source or to an early partitioning into an S-bearing fluid phase. The high Au/Cu ratio of sulfides formed as monosulfide solid solution may be associated with the potassic character of the magmas in this sector of the Central Andes.

Introduction

Porphyry copper ore deposits represent a primary source for Cu, Mo, and Au in the world and most porphyry-type systems are typically associated with subduction and postsubduction setting magmatism (Sillitoe, 2010; Richards, 2015). However, only a limited number of these magmatic systems generate economically exploitable ore deposits, whereas most are barren. Thus, understanding the factors that can cause a magmatic system to develop a porphyry ore deposit, or not, is critical for mineral exploration, as well as being a long-considered research subject.

The critical factors invoked to play a role in the chalcophile metal fertility of an arc magma include the metal endowment of the primary magma (McInnes et al., 1999; Mungall, 2002), the volume of magma involved and the duration of magmatic activity (Chelle-Michou et al., 2017; Chiaradia and Caricchi, 2017), the efficient transfer and precipitation of the metals carried by the magmatic fluid (Audétat and Simon, 2012, and references therein), and critically, the exsolution of a magmatic sulfide melt from the silicate melt (Halter et al., 2002, 2005; Audétat and Simon, 2012; Wilkinson, 2013; Park et al., 2015, 2019; Hao et al., 2019; Zhang and Audétat, 2017; Chang and Audétat, 2018; Georgatou et al., 2018; Georgatou and Chiaradia, 2020; Rottier et al., 2019; Costa et al., 2021). This latter factor is critical since chalcophile elements such as Cu and Au strongly partition to an exsolved sulfide melt, leaving the residual silicate melt depleted. As a consequence, the timing of sulfide melt exsolution with respect to magma differentiation and to fluid saturation can be critical in the evolution of fertile magmatic systems, with early sulfide saturation potentially limiting, in a significant way, the metal fertility of the magma (Richards, 2011; Park et al., 2015, 2019; Hao et al., 2019). However, early sulfide saturation and metal segregation within sulfide melts may also play an essential role in the preconcentration of ore metals at crustal levels, if they are later remobilized either by sulfur-undersaturated silicate melts or by sulfur- and chlorine-bearing magmatic aqueous fluids (Halter et al., 2002, 2005; Nadeau et al., 2010; Wilkinson, 2013; Zhang and Audétat, 2017). Sulfides stored in the lower parts of a magma chamber may, as recently demonstrated,

*Deceased June 29, 2015.
†Corresponding author: e-mail, paolo.fulignati@unipi.it

Open Access (CC-BY-NC) publication of the Jeremy P. Richards memorial volume was generously supported by BHP Metals Exploration and the Laurentian University Mineral Exploration Research Centre (MERC) and Harquail School of Earth Sciences (HES).

Digital Appendices are available online at www.segweb.org/SP24-Appendices.
doi: 10.5382/SP.24.07; 19 p.

become buoyant by attachment to low-density vapor bubbles to form sulfide droplets (Yao and Mungall, 2020), or remain at the bottom of the chamber, to be subsequently dissolved by magmatic-hydrothermal fluids that contribute to the formation of Cu-Au ores (Halter et al., 2002; Bai et al., 2020).

Variables associated with the tectono-magmatic setting also exert a role in ore-forming processes related to porphyry copper systems (Sillitoe, 2010). These include (1) the calc-alkaline/potassic affinity of the magmas; (2) the thickness of the crust in the overriding plate, favoring accumulation of Cu-bearing sulfides in thick arcs (Wilkinson, 2013; Chiaradia, 2014); (3) the debated link between adakitic magmas (either formed by crustal-level processes or slab melting) and metallogenic potential of arc regions (Richards and Kerrich, 2007, and references therein); and (4) the coincidence with slab shallowing induced by subduction of aseismic ridges (Kay and Mpodozis, 2002; Rosenbaum et al., 2005; Carrasquero et al., 2018). Given this complexity, the study of the mechanisms of sulfide saturation and metal scavenging from the silicate melt in nonmineralized and nonhydrothermally altered volcanic products in a similar setting to porphyry copper deposits may contribute to the understanding of how these systems formed.

This work presents compositional data on magmatic sulfide inclusions (MSIs) hosted in nonmineralized volcanic products of the late Miocene Rincón-Portezuelo de las Ánimas Volcanic Complex (Gonzalez et al., 2005; Vezzoli et al., 2011). This is the easternmost magmatic occurrence in the back arc of the southern Central Andes, at 27°S, corresponding to the location of the Pampean shallowing slab subduction (Kay and Coira, 2009). The region is at the intersection of the Tucuman east-northeast structure (Tucuman transfer zone; de Urreiztieta et al., 1996) and the eastern end of the Culumpajá lineament (Fig. 1), one of the regional crustal structures that cross the Andean orogen in a north-northwest–south-southeast orientation, and is argued to have influenced the location of the Neogene magmatism and related porphyry Cu ± Mo ± Au and epithermal Au mineralization (Sasso and Clark, 1998; Chernicoff et al., 2002; Richards et al., 2013). We discuss the composition of magmatic sulfides in these volcanic products, which are apparently barren in terms of metal enrichment, in the framework of their magmatic evolution, in order to examine the implications on the fertility of magmas formed in this tectono-magmatic setting. The composition of the MSIs of Rincón-Portezuelo de las Ánimas is furthermore discussed in comparison with that of MSIs found in the nearby and coeval Farallón Negro Volcanic Complex, which is associated with the world-class Bajo de la Alumbrera porphyry Cu-Au deposit. We end by discussing some ideas on the magmatic factors involved in the development of porphyry copper deposits.

Geologic Framework

The southern Central Andes tectonic setting is dominated by the subduction, since the Jurassic, of the Nazca oceanic plate under the South American continental plate. The presently active volcanic arc, consequence of the subduction setting, is located in correspondence of the Western Cordillera since the Miocene (Fig. 1). South of about 27°S, the subduction angle gradually decreases towards a configuration of flat slab (Kay et al., 1999; Ramos and Folguera, 2009) and the asthenospheric wedge is strongly reduced. The flat slab configuration developed in correspondence of the subduction of the aseismic Juan Fernandez ridge in the oceanic plate (Kay and Mpodozis, 2002; Kay and Coira, 2009). As a consequence, between 27°S and 33°S there is no volcanic activity (volcanic gap) since the Miocene (Cahill and Isacks, 1992). Several volcanic centers in the back arc mark the eastward migration and waning of volcanic activity at this latitude in the late Miocene

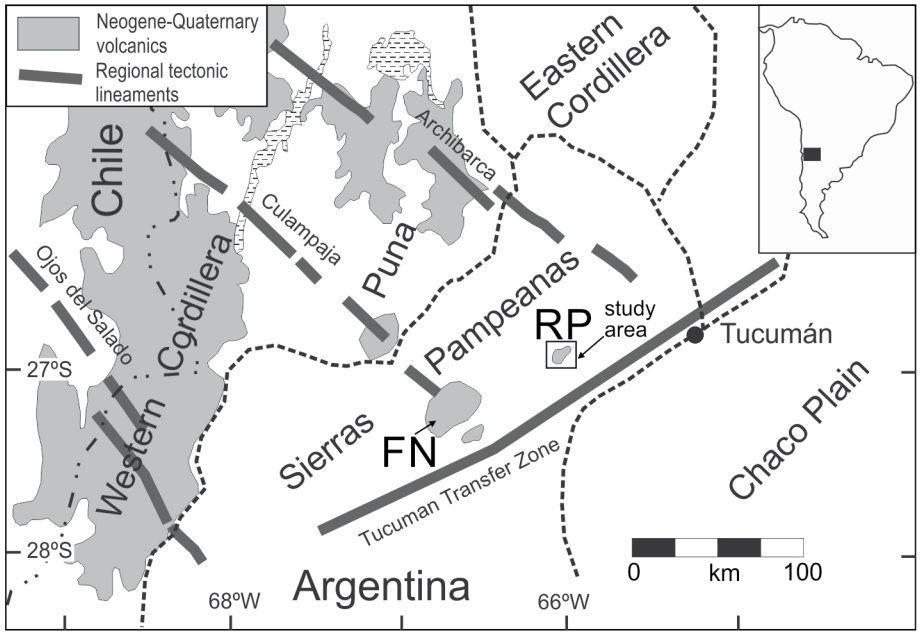

Fig. 1. Geologic sketch map of northwestern Argentina, showing the location of the Rincón-Portezuelo de las Ánimas (RP) and Farallón Negro (FN) Volcanic Complexes in relationship to regional-scale lineaments and Central Andes Miocene–Quaternary volcanism. The sampling area is indicated.

(Fig. 1). At the northeastern edge of the flat slab these include Farallón Negro (Sasso and Clark, 1998; Halter et al., 2005) and Rincón-Portezuelo de las Ánimas (Gonzalez et al., 2005; Vezzoli et al., 2011; Fig. 1).

The late Miocene (8–9 Ma; Vezzoli et al., 2011) Rincón-Portezuelo de las Ánimas volcanic field is located in the Sierras Pampeanas of northwest Argentina, at 26° 50'S and 65° 50'W (Fig. 1). Due to the shallowing of the subducting plate south of 27°S, during the Miocene the arc migrated to the east (Kay et al., 1999) and Rincón-Portezuelo de las Ánimas was the easternmost volcanic center at that latitude. The volcanic activity consisted of explosive and effusive eruptions leading to the building of a composite andesitic-dacitic central edifice, followed by basaltic trachyandesite to trachyandesite lava flows and scoria cones, which ended the volcanic activity in the area (González et al., 2005; Vezzoli et al., 2011, and in prep.). Deposits of debris avalanche indicate that the stratovolcano edifice was affected by a lateral collapse, preceding the final mafic lava flows (Vezzoli et al., 2011). Post-Miocene Andean tectonics deeply dismembered the volcanic succession and presently the remnants of the edifice are exposed at elevations of about 2,000 m apart. The chemical composition of the Rincón-Portezuelo de las Ánimas rocks covers a range from 52 to 63 wt % SiO_2 and, when plotted in a K_2O versus SiO_2 diagram (Fig. 2), crosses with nearly constant K_2O the boundary between the fields of the shoshonite and high K calc-alkaline series. The trace element composition of the Rincón-Portezuelo de las Ánimas rocks displays low Ta and Nb contents and high La/Ta and Ba/Nb ratios, indicating an evident arc imprint (Vezzoli et al., 2011).

Materials and Analytical Methods

The rock samples employed for this research have been collected during two field campaigns by L.V. and R.H.O. and full details on sampling and geology of the outcrops and on geochemistry of the samples are in a paper in preparation (Vezzoli et al., in prep.). Thirteen samples were selected to represent the compositional range of the Rincón-Portezuelo de las Ánimas products. Representative major and trace element data are reported in Appendix 1. From each sample, one to two polished thin sections were prepared (polishing in water) and examined under a dual reflected/transmitted light petrographic microscope. After carbon coating of thin sections, backscattered electron (BSE) imaging and energy dispersive spectrometry (EDS) microanalysis on 53 sulfide inclusions and a chalcopyrite reference material were carried out using a Quanta 450 FE-SEM equipped with a Bruker's QUANTAX EDS microanalysis with phi-rho-z EDS quantification (20-kV filament voltage, 10-mm working distance, up to 16,000× magnification, spot size 1.0 nm) housed in the University of Pisa (CISUP), Italy. Electron microprobe analyses on 21 sulfide inclusions and host minerals were performed on a JEOL 8200 Superprobe™ at the Department of Earth Sciences "Ardito Desio" of the University of Milan, Italy. Operating conditions were 15-kV accelerating voltage, 5-nA beam current, 3-μm beam size, and counting time of 20 s on peaks and 10 s in background. The following standards have been adopted: grossular (Si, Ca, Al), omphacite (Na), forsterite (Mg), fayalite (Fe), ilmenite (Ti), orthoclase (K), rhodonite (Mn), and Cr (pure element).

Laser ablation-inductively coupled plasma mass spectrometry (LA-ICPMS) analysis of the elements listed in Table 3 on 21 sulfide inclusions were performed at the Université de Montpellier (France), AETE-ISO regional facility of the OSU OREME, with a 193-nm pulsed ArF excimer laser (Analyte G2 from Teledyne) coupled to a Thermofinnigan XR mass spectrometer. Ablation experiments were conducted under ultrapure helium and the helium + particulate flow was subsequently mixed with pure N_2 to enhance further sensitivity. The spot size was 8 to 10 μm depending on the size of the sulfide and was chosen to ensure the best representativeness of the bulk sulfide. Fluence was set at 4.5 J/cm^2 with a frequency of 6 Hz. Examples of time-resolved laser ablation signals for types 1 and 2 MSIs are given in Appendix 2. The polymetallic sulfide MASS-1 reference material was used as an external standard and Fe was the internal standard (values from Georem at http://georem.mpch-mainz.gwdg.de/sample_query.asp). Ru and Os do not appear as certified values in the MASS standard certificate and they have not been analyzed in the present study. Ir was not analyzed. Data reduction was carried out with the Glitter software package (http://www.glitter-gemoc.com). The average of the MASS standard (n = 7) analyzed during the course of this study as well as standard deviation error expressed in % are provided in the data tables.

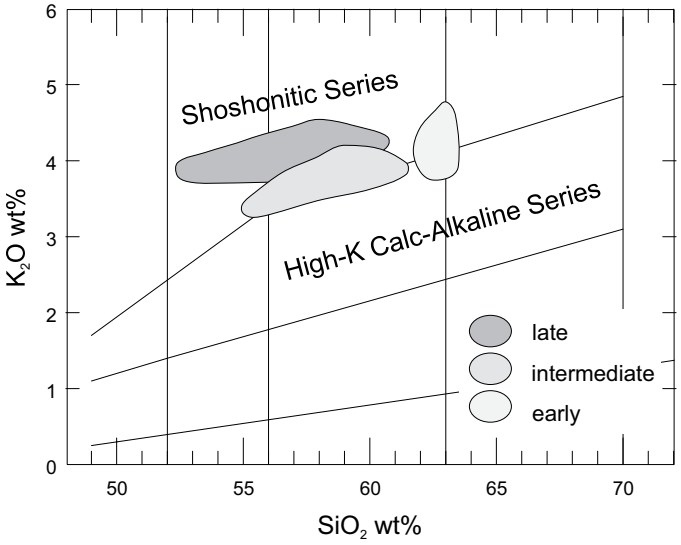

Fig. 2. Composition of the Rincón-Portezuelo de las Ánimas volcanic rocks, distinguished into three phases of volcanic activity (early, intermediate, and late), in the Peccerillo and Taylor (1976) classification diagram.

Results

Petrographic and compositional features of the Rincón-Portezuelo de las Ánimas volcanic rocks

The Rincón-Portezuelo de las Ánimas volcanic rocks studied in this work are mainly andesitic-trachyandesitic lavas, with high K dacite products belonging to the early phase of activity of the complex and basaltic trachyandesites erupted mainly in the last phase of activity. They are all porphyritic, with 15 to 35% phenocryst abundance (Table 1). Representative major element chemical analyses are reported in Appendix 1. The least evolved lavas are shoshonites in the K_2O versus

Table 1. Petrographic and Compositional Features of the Rincón-Portezuelo de las Ánimas Volcanic Rocks[1]

Sample no.	Volcanic phase	Classification	Mg #	Cu (ppm)	Presence of sulfide accessories
SA6	Early	High K dacite	41.8	10	None
SA10	Early	Shoshonitic basalt (hbl-rich crystal mush)	54.8	80	Abundant Cu-rich sulfides, rare pyrrhotite
PA13	Intermediate	High K andesite/latite	44.8	bdl	Pyrrhotite
PA1	Intermediate	Latite	46.3	10	Scarce pyrrhotite
SA7	Intermediate	Latite	49.2	10	Pyrrhotite
PA14	Intermediate	Latite	50.9	20	Pyrrhotite and rare unmixed Cu-rich pyrrhotite
PA15	Intermediate	Latite	51.2	20	Pyrrhotite and rare unmixed Cu-rich pyrrhotite
SA12	Intermediate	High K basaltic andesite/shoshonite	47.7	40	None
PA23	Late	Latite	44.3	bdl	Abundant pyrrhotite
PA20	Late	Latite	48.0	20	Abundant pyrrhotite
PA22	Late	Latite	49.7	30	Pyrrhotite
SA15	Late	Shoshonite	48.9	60	Scarce pyrrhotite
SA8	Late	Shoshonite	49.8	100	None

Abbreviation: bdl = below detectable level

[1] Classification and degree of evolution (Mg # = 100*Mg/Mg + Fe^{2+}, calculated with Fe_2O_3/FeO of 0.2 for basalt and 0.35 for latites and andesites (from Middlemost, 1989), bulk-rock Cu content and presence of sulfide inclusions in the studied samples; classification follows the K_2O vs. SiO_2 diagram of Peccerillo and Taylor (1976)

SiO_2 diagram of Peccerillo and Taylor (1976; Fig. 2) and have phenocrysts of olivine, clinopyroxene, and plagioclase, with clinopyroxene and plagioclase in the groundmass. The shoshonites of the late phase have a higher fraction of olivine in the phenocryst assemblage. Olivine is always absent in the groundmass. The rocks with intermediate degree of evolution fall in the latite field of the K_2O versus SiO_2 diagram (Fig. 2) and display a phenocryst assemblage dominated by plagioclase, clinopyroxene, and biotite with minor orthopyroxene (mainly in the intermediate phase). Olivine, when present, is rimmed by orthopyroxene, which, in some cases, is rimmed by clinopyroxene. Part of the samples contains abundant amphibole, which in some lavas has rounded corners, suggesting disequilibrium with the host magma. The groundmass is fine grained and consists of feldspars, clinopyroxene, and Ti-magnetite with, in some samples, devitrified volcanic glass. The main accessories are apatite and, in most samples, sulfides. Xenocrystic rounded quartz crystals or aggregates, sometimes with clinopyroxene fine-grained coronitic structures, are rather common. The high K dacites have phenocrysts of plagioclase and hornblende with minor sanidine and biotite and scarce pyroxene, in a hypocrystalline/hyalophylitic groundmass. Ti-magnetite and apatite occur as accessories. The deposits of the dacite explosive early phase contain a highly crystalline and unaltered enclave. The texture of the enclave is mostly equigranular, dominated by amphibole with minor plagioclase, Ti magnetite, and interstitial devitrified glass, with sparse vesicles (Fig. 3). This is interpreted as a cognate enclave, representing a fragment of the wall-rock crystal mush ejected by the most explosive phase recorded at Rincón-Portezuelo de las Ánimas.

The results of the study of thin sections under transmitted and reflected light for the determination of the petrographic features, presence, and characteristics of magmatic sulfides are summarized in Table 1. For the purpose of this study, 13 samples (12 lavas and the cognate enclave) have been selected from the early (two samples), intermediate (six samples), and late (five samples) phases of activity of the Rincón-Portezuelo de las Ánimas complex, to represent the variable degrees of magmatic chemical evolution and the variable potassic (high K calc-alkaline-shoshonitic) character of Rincón-Portezuelo de las Ánimas rocks. The lavas have Mg values (Mg# = Mg/(Mg + Fe^{2+}) and silica contents ranging from 51 to 41 and

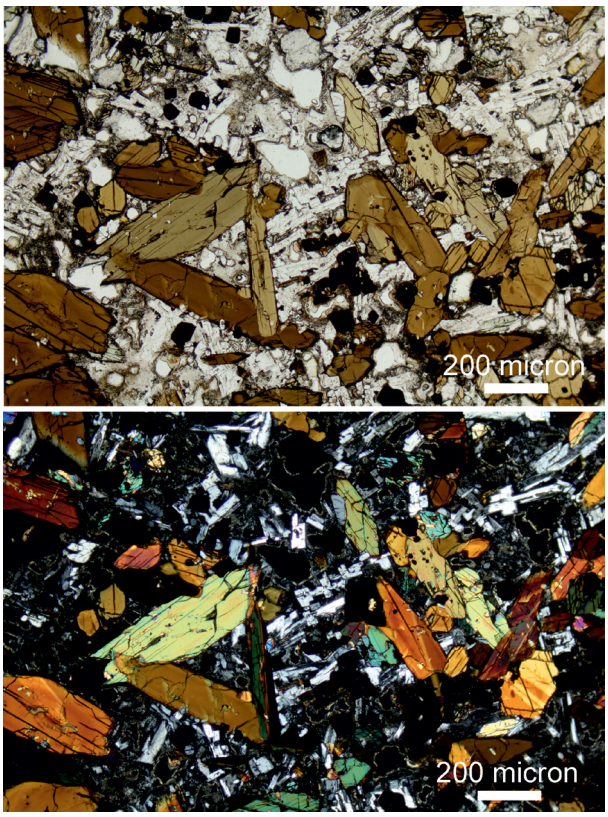

Fig. 3. Transmitted light (above) and crossed nicols (below) photomicrographs of the hornblende-rich cognate enclave.

from 52 to 62 wt %, respectively. The enclave bulk-rock composition is basaltic (shoshonitic basalt in the Peccerillo and Taylor, 1976, classification), with an Mg value of 54.8 (Table 1; App. 1); being the enclave of a fragment of an hornblende-rich crystal mush, its bulk-rock composition may not be representative of magma composition.

Magmatic sulfides: Microtextural observations and major and trace element composition

Magmatic sulfide inclusions in the Rincón-Portezuelo de las Ánimas volcanic products occur, with variable abundance, in all samples with intermediate evolution degree (latites), while they are rare or absent in the high K basaltic andesites and shoshonites and in high K dacites (Table 1). They are enclosed in phenocrysts and very rarely they can be found in the groundmass, partially resorbed. Under reflected light microscopy, the presence of different sulfide phases is suggested by the different reflected light color. Three types of MSIs (types 1–3) were identified based on the presence of unmixing textures and on the Cu-Fe-S composition. Their compositional and textural features are summarized in Table 2. The description and chemical composition of single sulfide inclusions are reported in Tables 3 and 4.

Type 1 MSIs are Cu rich and are abundant (i.e., 1–2 MSIs exposed in thin section in nearly half the phenocrysts) only in the hornblende-rich crystal-mush enclave (Tables 1, 2). They are 20 to 30 μm in mean diameter and are mainly trapped in hornblende and subordinately in plagioclase, sometimes with silicate glass or accessory mineral (apatite) inclusions. The sulfide inclusions display a polygonal shape recalling the negative shape of the host crystal (Fig. 4a-b). When the sulfide is in contact with glass (the trapped silicate melt), the boundary is, instead, curved (Fig. 4b). Type 1 MSIs often show unmixing textures, in the form of irregular veinlets or globules (Fig. 4b-d). Among those analyzed, 16 out of 27 type 1 sulfides are evidently unmixed (Table 3), and it cannot be excluded that some inclusions, which are homogeneous in two-dimensional images, are unmixed in the third dimension. The unmixed portions in form of veinlets represent 10 to 15% of the area of the exposed inclusion and have higher Cu content than the main sulfide phase. When plotted in a Cu-Fe-S diagram at 1,000°C (Fig. 5), the analyses of the single portions of type 1 MSIs span 18 to 55 wt % Cu, from bornite solid solution (bnss) across the sulfide liquid field, while the composition of the homogeneous (or apparently homogeneous) MSIs span 22 to 43 wt % Cu (Tables 2, 3). One-third of the unmixed inclusions contain Pb sulfide and more rarely Ag sulfide phases, in the form of tiny globules or thin rims (Fig. 4c-d; among those analyzed, 5 over 16 unmixed sulfide inclusions, Table 3).

Type 2 MSIs are homogeneous, mostly rounded, and are generally smaller than type 1 (Table 2; Fig. 4e-f); only one type 2 MSI with fine postentrapment unmixing has been found (Fig. 4g). They are hosted within clinopyroxene and rarely in hornblende and orthopyroxene and show a Cu content that is between 0.1 up to about 9 wt % (Table 2). Type 2 MSIs plot within or close to the field of monosulfide solid solution in the Cu-Fe-S diagram at 1,000°C (mss, Fig. 5). They are common in most lavas and particularly abundant (i.e., one to two up to six MSIs per phenocryst, exposed in thin section in most phenocrysts) in the latites of the late phase. A few type 2 MSIs have been also found in the hornblende-rich enclave, although not in the same phenocrysts with type 1. As a consequence, types 1 and 2 MSIs may be, or not, trapped at the same crystallization stage in the hornblende-rich enclave.

Type 3 MSIs (Table 2) are represented by four sulfides found only in two lava samples. These are unmixed sulfide inclusions composed of pyrrhotite (mss field, Fig. 5) and a sulfide having higher Cu content, between 23 and 31 wt % (Fig. 5; Tables 2, 3). In one inclusion the unmixed portion is an Ni-rich sulfide (Fig. 4h).

With the aim to constrain the bulk composition (particularly the trace element and metal content) of MSIs, these (types 1 and 2) were analyzed by LA-ICPMS and the results are reported in Table 4. The mean of types 1 and 2 MSIs and their maximum and minimum values above detection limit are also reported in Table 4. Unfortunately, the paucity and small size of type 3 MSIs did not allow the LA-ICPMS analysis.

The composition of trace elements measured on types 1 and 2 MSIs displays notable differences (Figs. 6a, 7). In addition to having higher Cu content, type 1 MSIs show higher Rh, Se, Pt, Ag, Te, Cd, Tl, Pb, and Bi and lower Sb and Mo content, whereas Co, Ni, Au, and Pd have a similar range of contents. Lead and Cd are positively correlated with Cu in type 2 MSIs, whereas they show higher values and a large variation in type 1 MSIs (Fig. 7a, c). Overall, general positive correlations with Cu exist for Pb and Cd, and very roughly for Ag (Fig. 7a-c). However, Cu and Au are not correlated (Fig. 7d). Bismuth shows a good positive correlation with Pb both in types 1 and 2 MSIs (Fig. 7e). The variability in the concentrations of these metals, in particular Pb and Ag, in type 1 MSIs could reflect a variable composition of the trapped sulfide liquid, or the effect of the tiny Pb-rich globules (1-2 μm size) being included/excluded by the 10-μm laser ablation spot (see Fig. 4c-d, Table 3). The very good

Table 2. Characteristics of the Three Types of Sulfide Inclusions (MSIs) Found in the Rincón-Portezuelo de las Ánimas Studied Samples and Their Host Minerals and Rocks (the complete list of sulfides is reported in Table 3)

Sulfide inclusion types	Morphology	Size (µm, avg and min-max)	Sulfide phase(s)	Wt % Cu[1]	Host rocks and volcanic phase	Host minerals
Type 1	Polygonal	23 (5–35)	Unmixed; bn, cp, cb, Pb- and Ag-phases	18–55	Hbl-rich enclave in phase 1 volcanics	Hbl, pl
Type 2	Rounded	12 (3–25)	Mostly homogeneous; po	0.1–9	Andesitic and latitic lavas of all volcanic phases; rarely in hbl-rich enclave	Cpx, opx, hbl
Type 3	Rounded	9 (5–10)	Unmixed; po, cb, cp	0.1–31	andesitic lavas of phase 2	Cpx, opx

Abbreviations: bn = bornite, cb = cubanite, cp = chalcopyrite, hbl = hornblende, opx = orthopyroxene, pl = plagioclase, po = pyrrhotite
[1] Range of Cu covered by the Cu phases in each sulfide type (data in Table 3)

Table 3. Characteristics and Major Element Composition of the Sulfide Inclusions Analyzed by EPMA and EDS[1]

Host rock id	Sulfide id	Sulfide type	Size (micron)	Host mineral	Sulfide description	EPMA/ EDS[2]	Fe (wt %)	S	Co	Ni	Zn	Cu
SA 10	s1	1	25x25	Hbl	Polygonal, homogeneous	EPMA	33.03	34.08	0.04	0.06	bdl	30.33
SA 10	s2	1	30x20	Hbl	Unmixed with Pb-rich 3x3 micron globule	EPMA	42.22	35.37	0.23	0.52	bdl	18.13
SA 10	s2	1	30x20	Hbl	Unmixed 2	EPMA	9.78	18.58	0.04	0.13	bdl	6.70
SA 10	s3	1	20x20	Hbl	Polygonal	EPMA	23.14	31.58	0.03	0.41	bdl	42.84
SA 10	s4	1	20x20	Hbl	Polygonal, unmixed	EPMA	15.18	27.83	0.00	bdl	bdl	55.24
SA 10	s4	1	20x20	Hbl	Unmixed 2	EPMA	29.26	34.59	0.07	0.09	bdl	34.65
SA 10	s5	1	30x20	Hbl	Homogeneous, curved boundaries with co-trapped glass	EPMA	36.28	34.65	0.08	0.12	bdl	25.82
SA 10	s6	1	25x25	Hbl	Polygonal, unmixed	EPMA	32.90	35.17	0.09	0.05	bdl	29.47
SA 10	s7	1	20x20	Hbl	Homogeneous	EPMA	43.37	34.84	0.29	0.54	bdl	22.09
SA 10	s8	1	25x25	Hbl	Unmixed	EPMA	30.50	33.15	0.08	0.18	bdl	35.33
SA 10	s8	1	25x25	Hbl	Unmixed 2	EPMA	24.94	29.26	0.03	0.04	bdl	43.06
SA 10	s19	1	20x20	Hbl	Unmixed, with Pb-rich globule	EPMA	33.85	35.01	0.08	0.14	bdl	29.10
SA 10	s20	1	20x20	Hbl	Unmixed, with Pb-rich globule	EPMA	32.16	34.16	0.01	0.09	bdl	31.42
SA 10	s21	1	20x20	Hbl	Unmixed, with lamellae	EPMA	33.51	34.81	0.09	0.22	bdl	30.36
PA 20	s9	2	10x10	Cpx	Homogeneous	EPMA	59.17	40.19	0.23	0.35	bdl	0.15
PA 20	s10	2	5x5	Cpx	Homogeneous	EPMA	59.85	39.73	0.23	0.21	bdl	0.05
PA 20	s11	2	5x5	Cpx	Homogeneous	EPMA	59.32	39.99	0.23	0.85	bdl	0.01
PA 20	s12	2	10x10	Cpx	Homogeneous, trapped with melt	EPMA	59.80	40.36	0.20	0.17	bdl	0.10
PA 20	s13	2	10x10	Hbl	Homogeneous, irregular shape	EPMA	59.83	40.32	0.15	0.17	bdl	0.06
PA 14	s14	2	10x10	Cpx	Homogeneous, rounded	EPMA	59.80	38.85	0.18	0.32	bdl	0.11
PA 14	s15	2	10x10	Opx	Homogeneous, irregular shape	EPMA	60.57	38.91	0.10	0.13	bdl	0.20
PA 14	s16	2	10x10	Cpx	Homogeneous/unmixed? rounded shape	EPMA	53.80	38.63	0.22	0.33	bdl	9.10
PA 14	s17	2	10x10	Cpx	Homogeneous, rounded	EPMA	59.29	39.66	0.22	0.40	bdl	0.03
PA 14	s18	2	10x10	Cpx	Homogeneous, rounded	EPMA	59.03	39.76	0.15	0.33	bdl	0.15
SA 10	m1	1	30x30	Hbl	Polygonal homogeneous	EDS	34.14	34.21	bdl	0.00	bdl	31.64
SA 10	m2	1	10x10	Hbl	Polygonal; unmixed	EDS	33.70	35.00	bdl	0.00	bdl	31.30
SA 10	m2	1	10x10	Hbl	Unmixed 2	EDS	33.58	31.33	bdl	0.00	bdl	35.10
SA 10	m3	1	15x15	Hbl	Polygonal, Pb-rich unmixing	EDS	34.27	33.13	bdl	0.00	bdl	32.60
SA 10	m3	1	15x15	Hbl	Unmixed 2	EDS	10.12	13.73	bdl	0.00	bdl	6.85
SA 10	m3	1	15x15	Hbl	Unmixed 3	EDS	20.84	19.65	bdl	0.00	bdl	11.90
SA 10	m4	1	3x3	Pl	Polygonal homogeneous	EDS	35.53	32.05	bdl	0.00	bdl	32.42
SA 10	m5	1	35x35	Hbl	Polygonal, Pb-rich unmixing	EDS	34.52	35.43	bdl	0.00	bdl	30.05
SA 10	m5	1			Unmixed 2	EDS	25.94	19.20	bdl	0.00	bdl	14.41
SA 10	m6	1	30x30	Hbl	Polygonal, unmixed with Cu-rich and Ag-rich sulfides	EDS	34.19	31.49	bdl	0.00	bdl	34.32
SA 10	m6	1	30x30	Hbl	Unmixed 2	EDS	24.74	29.92	bdl	0.00	bdl	45.34
SA 10	m6	1	30x30	Hbl	Unmixed 3	EDS	24.65	21.04	bdl	0.00	bdl	26.45
SA 10	m7	1	20x20	Hbl	Polygonal	EDS	32.69	33.30	bdl	0.00	bdl	34.00
SA 10	fs1	1	30x20	Hbl	Polygonal, unmixed trapped with glass and apatite	EDS	27.85	31.11	bdl	0.15	bdl	40.10
SA 10	fs2	1	20x10	Hbl	Polygonal, Pb-rich unmixing	EDS	36.72	33.20	0.22	0.37	bdl	29.49
SA 10	fs2	1	20x10	Hbl	Unmixed 2	EDS	43.42	0.00	bdl	0.00	bdl	37.48
SA 10	fs3	1	20x15	Hbl	Polygonal, unmixed	EDS	34.73	33.06	bdl	0.00	bdl	32.21
SA 10	fs4	1	30x20	Hbl	Polygonal homogeneous	EDS	34.68	32.51	bdl	0.00	bdl	32.81
SA 10	fs6	1	20x10	Hbl	Polygonal homogeneous	EDS	37.27	34.84	bdl	0.00	bdl	27.89
SA 10	fs7	1	15x10	Hbl	Polygonal homogeneous	EDS	34.34	29.95	bdl	0.33	bdl	35.38
SA 10	fs8	1	25x20	Hbl	Polygonal, unmixed	EDS	38.16	33.07	bdl	0.00	bdl	28.77
SA 10	fs9	1	25x20	Hbl	Unmixed 2	EDS	35.15	32.18	bdl	0.00	bdl	32.67
SA 10	fs9	1	25x20	Hbl	Unmixed 3	EDS	27.41	30.12	bdl	0.00	bdl	42.47
SA 10	fs11	1	30x20	Hbl	Polygonal, unmixed	EDS	32.53	30.48	bdl	0.00	bdl	36.98
SA 10	fs10	2	20x20	Hbl	Homogeneous, approx. rounded	EDS	60.25	39.75	bdl	0.00	bdl	bdl
SA 10	fs12	2	25x20	Hbl	Homogeneous, irregular/ amoeboid shape	EDS	64.25	35.75	bdl	0.00	bdl	bdl
PA 13	m8	2	6x6	Cpx	Homogeneous, rounded	EDS	61.07	38.63	bdl	0.00	bdl	0.30
PA 13	m34	2	3x3	Cpx	Homogeneous, rounded	EDS	62.82	32.98	2.16	0.15	bdl	1.89
PA 13	m35	2	3x3	Cpx	Homogeneous, rounded	EDS	63.45	31.97	0.89	0.00	bdl	3.69
PA 13	m9	2	8x8	Cpx	Homogeneous, rounded	EDS	61.57	36.16	2.22	0.00	bdl	0.05
PA 20	m10	2	15x15	Cpx	Homogeneous, rounded	EDS	63.90	35.53	0.35	0.22	bdl	bdl
PA 20	m11	2	10x10	Cpx	Homogeneous, polygonal	EDS	60.05	38.87	0.48	0.50	bdl	0.09
PA 20	m12	2	7x10	Cpx	Homogeneous, rounded, irregular shape	EDS	62.04	37.96	bdl	0.00	bdl	bdl
PA 20	m13	2	10x15	Cpx	Homogeneous, rounded	EDS	62.75	36.40	0.57	0.27	bdl	bdl
PA 20	m14	2	5x5	Cpx	Homogeneous, rounded	EDS	62.03	37.10	0.44	0.09	bdl	0.34
PA 20	m15	2	5x5	Cpx	Homogeneous, rounded	EDS	62.02	37.51	0.42	0.05	bdl	bdl
PA 20	m16	2	5x10	Cpx	Homogeneous, rounded	EDS	63.19	36.38	0.43	0.00	bdl	bdl

Table 3. *(Cont.)*

Host rock id	Ag	Pb	total	Classification[3]	Fe (at %)	S	Co	Ni	Zn	Cu	Ag	Pb	Fe/ (S+Fe)
SA 10	0.02	0.14	97.69	Cb-Cp	28.54	47.85	0.03	0.05	0.00	23.49	0.01	0.04	0.37
SA 10	bdl	0.13	96.59	Po-Cb	36.18	49.25	0.19	0.41	0.00	13.93	0.00	0.03	0.42
SA 10	bdl	55.89	91.12	Pb-sulfide	15.31	47.28	0.06	0.19	0.00	9.41	0.00	27.75	0.24
SA 10	0.08	0.03	98.11	Cp-Bn	20.42	45.28	0.03	0.33	0.00	33.89	0.04	0.01	0.31
SA 10	bdl	0.07	98.32	Cp-Bn	13.81	41.13	0.00	0.00	0.00	45.04	0.00	0.02	0.25
SA 10	0.01	0.08	98.75	Cp	25.07	48.16	0.06	0.07	0.00	26.62	0.01	0.02	0.34
SA 10	bdl	0.12	97.07	Cb-Cp	31.29	48.55	0.07	0.10	0.00	19.96	0.00	0.03	0.39
SA 10	bdl	0.05	97.74	Cb-Cp	28.21	49.00	0.08	0.04	0.00	22.65	0.00	0.01	0.37
SA 10	0.03	0.09	101.24	Cb	35.96	46.94	0.23	0.41	0.00	16.42	0.01	0.02	0.43
SA 10	0.00	0.15	99.39	Cp-Bn	26.22	46.31	0.06	0.14	0.00	27.23	0.00	0.04	0.36
SA 10	bdl	1.39	98.73	Cp-Bn	22.35	42.60	0.03	0.04	0.00	34.59	0.00	0.39	0.34
SA 10	bdl	0.04	98.22	Cb-Cp	28.92	48.60	0.06	0.11	0.00	22.29	0.00	0.01	0.37
SA 10	0.00	0.01	97.84	Cb-Cp	27.74	47.88	0.00	0.07	0.00	24.30	0.00	0.00	0.37
SA 10	0.04	0.17	99.20	Cb-Cp	28.48	48.08	0.07	0.17	0.00	23.13	0.02	0.05	0.37
PA 20	bdl	0.09	100.17	Po	47.27	52.17	0.17	0.26	0.00	0.11	0.00	0.02	0.48
PA 20	bdl	0.19	100.25	Po	47.91	51.68	0.18	0.15	0.00	0.03	0.00	0.05	0.48
PA 20	0.00	0.02	100.42	Po	47.33	51.85	0.18	0.63	0.00	0.01	0.00	0.00	0.48
PA 20	0.01	0.16	100.80	Po	47.51	52.10	0.16	0.12	0.00	0.07	0.00	0.04	0.48
PA 20	0.01	0.11	100.65	Po	47.58	52.10	0.12	0.12	0.00	0.04	0.00	0.03	0.48
PA 14	0.05	0.09	99.40	Po	48.40	51.09	0.14	0.24	0.00	0.08	0.02	0.02	0.49
PA 14	0.03	0.04	99.98	Po	48.76	50.90	0.08	0.10	0.00	0.15	0.01	0.01	0.49
PA 14	bdl	0.04	102.11	Po-Cb	42.95	50.12	0.17	0.24	0.00	6.51	0.00	0.01	0.46
PA 14	bdl	0.15	99.75	Po	47.66	51.81	0.17	0.30	0.00	0.02	0.00	0.04	0.48
PA 14	0.01	0.23	99.66	Po	47.49	51.98	0.11	0.25	0.00	0.11	0.01	0.06	0.48
SA 10	bdl	bdl	100.0	Cb-Cp	28.91	47.07	0.00	0.00	0.00	24.02	0.00	0.00	0.38
SA 10	bdl	bdl	100.0	Cb-Cp	28.41	47.94	0.00	0.00	0.00	23.65	0.00	0.00	0.37
SA 10	bdl	bdl	100.0	Cp	28.96	43.90	0.00	0.00	0.00	27.14	0.00	0.00	0.40
SA 10	bdl	bdl	100.0	Cb-Cp	29.21	45.88	0.00	0.00	0.00	24.91	0.00	0.00	0.39
SA 10	bdl	69.30	100.0	Pb-Cu-sulfide	16.71	36.85	0.00	0.00	0.00	10.14	0.00	36.29	0.31
SA 10	bdl	47.61	100.0	Pb-Cu-sulfide	26.53	40.66	0.00	0.00	0.00	13.58	0.00	19.22	0.39
SA 10	bdl	bdl	100.0	Cb--Cp	30.45	44.64	0.00	0.00	0.00	24.91	0.00	0.00	0.41
SA 10	bdl	bdl	100.0	Cb--Cp	29.00	48.37	0.00	0.00	0.00	22.63	0.00	0.00	0.37
SA 10	bdl	40.45	100.0	Pb-Cu-sulfide	31.30	37.64	0.00	0.00	0.00	15.59	0.00	15.47	0.45
SA 10	bdl	bdl	100.0	Cp	29.44	44.06	0.00	0.00	0.00	26.50	0.00	0.00	0.40
SA 10	bdl	bdl	100.0	Cp-Bn	21.70	42.65	0.00	0.00	0.00	35.65	0.00	0.00	0.34
SA 10	27.86	bdl	100.0	Ag-Cu-sulfide	25.16	34.90	0.00	0.00	0.00	24.21	15.73	0.00	0.42
SA 10	bdl	bdl	100.0	Cp	27.87	46.14	0.00	0.00	0.00	25.99	0.00	0.00	0.38
SA 10	bdl	0.79	100.0	Cp-Bn	23.68	46.06	0.00	0.12	0.00	29.96	0.00	0.18	0.34
SA 10	bdl	bdl	100.0	Cb-Cp	30.35	47.77	0.17	0.29	0.00	21.42	0.00	0.00	0.39
SA 10	bdl	19.10	100.0	Pb-Cu-sulfide	53.27	0.00	0.00	0.00	0.00	40.41	0.00	6.32	1.00
SA 10	bdl	bdl	100.0	Cb-Cp	28.80	47.73	0.00	0.00	0.00	23.47	0.00	0.00	0.38
SA 10	bdl	bdl	100.0	Cb-Cp	28.87	47.13	0.00	0.00	0.00	24.00	0.00	0.00	0.38
SA 10	bdl	bdl	100.0	Cb-Cp	30.44	49.55	0.00	0.00	0.00	20.02	0.00	0.00	0.38
SA 10	bdl	bdl	100.0	Cp-Bn	29.13	44.23	0.00	0.27	0.00	26.37	0.00	0.00	0.40
SA 10	bdl	bdl	100.0	Cb-Cp	31.53	47.58	0.00	0.00	0.00	20.89	0.00	0.00	0.40
SA 10	bdl	bdl	100.0	Cb-Cp	29.32	46.74	0.00	0.00	0.00	23.94	0.00	0.00	0.39
SA 10	bdl	bdl	100.0	Cp-Bn	23.39	44.76	0.00	0.00	0.00	31.85	0.00	0.00	0.34
SA 10	bdl	bdl	100.0	Cp-Bn	27.55	44.94	0.00	0.00	0.00	27.51	0.00	0.00	0.38
SA 10	bdl	bdl	100.0	Po	46.54	53.46	0.00	0.00	0.00	0.00	0.00	0.00	0.47
SA 10	bdl	bdl	100.0	Po	50.79	49.21	0.00	0.00	0.00	0.00	0.00	0.00	0.51
PA 13	bdl	bdl	100.0	Po	49.20	50.58	0.00	0.00	0.00	0.22	0.00	0.00	0.49
PA 13	bdl	bdl	100.0	Po-Cb	52.20	44.54	1.73	0.12	0.00	1.41	0.00	0.00	0.54
PA 13	bdl	bdl	100.0	Po-Cb	53.07	43.45	0.72	0.00	0.00	2.77	0.00	0.00	0.55
PA 13	bdl	bdl	100.0	Po	50.26	47.96	1.74	0.00	0.00	0.04	0.00	0.00	0.51
PA 20	bdl	bdl	100.0	Po	52.30	47.26	0.28	0.17	0.00	0.00	0.00	0.00	0.53
PA 20	bdl	bdl	100.0	Po	48.34	50.85	0.37	0.37	0.00	0.07	0.00	0.00	0.49
PA 20	bdl	bdl	100.0	Po	50.15	49.85	0.00	0.00	0.00	0.00	0.00	0.00	0.50
PA 20	bdl	bdl	100.0	Po	51.14	48.21	0.45	0.21	0.00	0.00	0.00	0.00	0.51
PA 20	bdl	bdl	100.0	Po	50.38	48.96	0.34	0.07	0.00	0.25	0.00	0.00	0.51
PA 20	bdl	bdl	100.0	Po	50.25	49.38	0.33	0.04	0.00	0.00	0.00	0.00	0.50
PA 20	bdl	bdl	100.0	Po	51.49	48.18	0.34	0.00	0.00	0.00	0.00	0.00	0.52

Table 3. *(Cont.)*

Host rock id	Sulfide id	Sulfide type	Size (micron)	Host mineral	Sulfide description	EPMA/ EDS[2]	Fe (wt %)	S	Co	Ni	Zn	Cu
PA 20	m17	2	10x10	Cpx	Homogeneous, rounded	EDS	61.47	37.71	0.39	0.31	bdl	0.12
PA 20	m18	2	10x10	Cpx	Homogeneous, amoeboid	EDS	61.81	38.19	bdl	0.00	bdl	bdl
PA 20	m19	2	10x10	Cpx	Homogeneous, amoeboid	EDS	58.14	40.64	0.45	0.62	bdl	0.14
PA 20	ls1	2	35x20	Cpx	Homogeneous, rounded	EDS	62.72	37.28	bdl	bdl	bdl	bdl
PA 20	ls2	2	10x10	Cpx	Homogeneous, rounded	EDS	63.53	36.47	bdl	bdl	bdl	bdl
PA 20	ls3	2	10x10	Cpx	Homogeneous, rounded	EDS	57.75	39.13	bdl	bdl	bdl	3.12
PA 20	ls4	2	15x10	Cpx	Homogeneous, rounded	EDS	64.08	35.92	bdl	bdl	bdl	bdl
PA 20	ls5	2	15x15	Cpx	Homogeneous, rounded	EDS	64.13	35.87	bdl	bdl	bdl	bdl
PA 20	ls6	2	10x10	Cpx	Homogeneous, rounded	EDS	62.20	37.80	bdl	bdl	bdl	bdl
PA 20	ls7	2	10x5	Cpx	Homogeneous, rounded	EDS	63.07	36.93	bdl	bdl	bdl	bdl
PA 20	ls9	2	20x15	Cpx	Homogeneous, rounded	EDS	60.93	39.07	bdl	bdl	bdl	bdl
PA 20	ls10	2	5x5	Cpx	Homogeneous, rounded	EDS	62.05	37.95	bdl	bdl	bdl	bdl
PA 20	ls12	2	10x10	Cpx	Homogeneous, rounded	EDS	62.65	37.35	bdl	bdl	bdl	bdl
PA 23	m20	2	10x10	Cpx	Homogeneous, rounded	EDS	59.89	34.72	0.53	0.12	bdl	4.74
PA 23	m36	2	5x15	Cpx	Homogeneous, rounded	EDS	63.67	35.11	0.51	0.17	bdl	0.54
PA 23	m21	2	8x10	Cpx	Homogeneous, rounded	EDS	61.30	37.81	0.37	0.49	bdl	0.03
PA 23	m22	2	5x10	Cpx	Homogeneous, rounded	EDS	62.16	36.91	0.29	0.37	bdl	0.27
PA 23	m23	2	5x5	Cpx	Homogeneous, rounded	EDS	64.10	35.00	0.47	0.00	bdl	0.43
SA 7	m24	2	20x15	Cpx	Homogeneous, amoeboid	EDS	62.08	37.49	bdl	0.43	bdl	0.00
SA 7	m25	2	10x10	Cpx	Homogeneous, rounded	EDS	61.64	38.22	bdl	0.14	bdl	0.00
SA 7	m27	2	5x5	Cpx	Homogeneous, rounded	EDS	63.61	35.77	bdl	0.40	bdl	0.22
SA 7	m28	2	5x5	Cpx	Homogeneous, rounded	EDS	62.63	36.70	bdl	0.45	bdl	0.22
SA 15	m29	2	5x5	Cpx	Homogeneous, rounded	EDS	56.63	39.15	bdl	0.13	bdl	4.09
PA 15	m30	3	5x10	Opx	Rounded, unmixed	EDS	63.52	35.42	bdl	0.94	bdl	0.12
PA 15	m30	3	5x10	Opx	Unmixed 2	EDS	38.35	34.66	bdl	24.29	bdl	2.70
PA 15	m30	3	5x10	Opx	Unmixed 3	EDS	33.78	33.97	bdl	1.19	bdl	31.06
PA 15	m31	3	10x10	Cpx	Rounded, unmixed	EDS	59.71	35.88	bdl	0.36	bdl	4.05
PA 15	m31	3	10x10	Cpx	Unmixed 2	EDS	44.36	31.51	bdl	0.27	bdl	23.86
PA 14	m32	3	10x10	Cpx	Rounded, unmixed	EDS	62.85	34.33	bdl	0.39	bdl	2.43
PA 14	m32	3	10x10	Cpx	Unmixed 2	EDS	45.71	31.34	bdl	bdl	bdl	22.95
PA 14	m33	3	10x10	Cpx	Rounded, amoeboid, unmixed	EDS	63.56	35.28	bdl	0.43	bdl	0.73
PA 14	m33	3	10x10	Cpx	Unmixed 2	EDS	57.72	34.27	bdl	0.35	bdl	7.66

[1] The unmixed globules and veins were analyzed when permitted by the size of the exposed surface; the analyses are classified as Po = Cu <1 wt %, Po-Cb = 1–22 wt %, Cb = 22–24 wt %, Cb-Cp = 24–33 wt %, Cp = 33–35 wt %, Cp-Bn = 35–62 wt %, Bn = Cu >62 wt %, following Georgatou et al. (2018) ; see Table 2 for abbreviations

[2] EDS analyses are normalized to 100 by the software used

[3] Classification based on Cu content following Georgatou et al. (2018)

correlation between Bi and Pb suggests that Bi may follow Pb, both during sulfide exsolution from magma and during the unmixing of the tiny globules in type 1 MSIs (Fig. 7d). The two analyzed type 2 sulfides found to coexist in the same rock with type 1 sulfides show concentrations similar to the entire type 2 population (Table 4, Figs. 6b, 7). When comparing types 1 and 2 inclusions with respect to the Cu-normalized composition, we observe that the $C_{element}/C_{Cu}$ ratios are higher in type 2 than in type 1 MSIs. Only Pb and Bi diverge from this general behavior having higher ratios in type 1 than in type 2 MSIs. (Fig. 6c).

Oxybarometry and thermobarometry

In order to constrain the crystallization conditions of the magmas that were stored in the Rincón-Portezuelo de Las Ánimas volcanic plumbing system, we used a variety of oxybarometers, thermometers, and barometers with the composition of the amphibole and clinopyroxene minerals hosting the sulfides (Table 5). The composition of the bulk rock was taken as representative of the silicate melt in equilibrium with the minerals (App. 1). The results are summarized in Table 6.

To determine the oxygen fugacity of the different investigated rocks, we used the Ridolfi et al. (2010) empirical equation based on amphibole composition. The calculated oxygen fugacity ranges from ΔNNO 0.4 to 0.7 for the hornblende-rich enclave and is around 0.6 for the latite lavas.

Pressure conditions have been estimated using three different barometers: Ridolfi et al. (2010) based on amphibole composition; Putirka et al. (2003) based on clinopyroxene-liquid equilibrium; and Neave and Putirka (2017) based on clinopyroxene-liquid equilibrium (Table 6). The obtained pressures are between 460 and 550 MPa for the hornblende-rich enclave and between 240 and 630 for latite lavas. Pressure estimation with amphibole composition of PA-20 sample (515 MPa) is in agreement with the pressure calculated with clinopyroxene-liquid barometers, falling within the range 300 to 630 MPa (Table 6).

In the hornblende-rich enclave, the two applied amphibole thermometers (Ridolfi et al., 2010; Putirka, 2016) give values that are generally in agreement within their associated uncertainties (±30°C for Putirka, 2016, thermometer and ±22°C for Ridolfi et al., 2010, thermometer) and are around 960° to 1,000°C (Table 6). The amphibole thermometers applied to the PA-20 lava sample give temperature values of 958° and 996°C, which are in the range of those calculated for the hornblende-rich enclave. Clinopyroxene-liquid thermometry on latitic lava samples indicates higher temperatures than those calculated for the hornblende-rich enclave and for amphibole

Table 3. *(Cont.)*

Host rock id	Ag	Pb	total	Classification[3]	Fe (at %)	S	Co	Ni	Zn	Cu	Ag	Pb	Fe/ (S+Fe)
PA 20	bdl	bdl	100.0	Po	49.77	49.61	0.30	0.23	0.00	0.09	0.00	0.00	0.50
PA 20	bdl	bdl	100.0	Po	49.90	50.10	0.00	0.00	0.00	0.00	0.00	0.00	0.50
PA 20	bdl	bdl	100.0	Po	46.39	52.70	0.35	0.46	0.00	0.10	0.00	0.00	0.47
PA 20	bdl	bdl	100.0	Po	49.14	50.86	0.00	0.00	0.00	0.00	0.00	0.00	0.49
PA 20	bdl	bdl	100.0	Po	50.01	49.99	0.00	0.00	0.00	0.00	0.00	0.00	0.50
PA 20	bdl	bdl	100.0	Po-Cb	44.90	52.97	0.00	0.00	0.00	2.13	0.00	0.00	0.46
PA 20	bdl	bdl	100.0	Po	50.61	49.39	0.00	0.00	0.00	0.00	0.00	0.00	0.51
PA 20	bdl	bdl	100.0	Po	50.66	49.34	0.00	0.00	0.00	0.00	0.00	0.00	0.51
PA 20	bdl	bdl	100.0	Po	48.59	51.41	0.00	0.00	0.00	0.00	0.00	0.00	0.49
PA 20	bdl	bdl	100.0	Po	49.52	50.48	0.00	0.00	0.00	0.00	0.00	0.00	0.50
PA 20	bdl	bdl	100.0	Po	47.25	52.75	0.00	0.00	0.00	0.00	0.00	0.00	0.47
PA 20	bdl	bdl	100.0	Po	48.43	51.57	0.00	0.00	0.00	0.00	0.00	0.00	0.48
PA 20	bdl	bdl	100.0	Po	49.07	50.93	0.00	0.00	0.00	0.00	0.00	0.00	0.49
PA 23	bdl	bdl	100.0	Po-Cb	49.42	46.56	0.42	0.09	0.00	3.50	0.00	0.00	0.51
PA 23	bdl	bdl	100.0	Po	52.25	46.82	0.41	0.13	0.00	0.40	0.00	0.00	0.53
PA 23	bdl	bdl	100.0	Po	49.60	49.72	0.29	0.37	0.00	0.02	0.00	0.00	0.50
PA 23	bdl	bdl	100.0	Po	50.54	48.76	0.23	0.28	0.00	0.20	0.00	0.00	0.51
PA 23	bdl	bdl	100.0	Po	52.62	46.70	0.37	0.00	0.00	0.31	0.00	0.00	0.53
SA 7	bdl	bdl	100.0	Po	50.31	49.37	0.00	0.32	0.00	0.00	0.00	0.00	0.50
SA 7	bdl	bdl	100.0	Po	49.76	50.14	0.00	0.10	0.00	0.00	0.00	0.00	0.50
SA 7	bdl	bdl	100.0	Po	52.01	47.53	0.00	0.30	0.00	0.16	0.00	0.00	0.52
SA 7	bdl	bdl	100.0	Po	50.97	48.53	0.00	0.34	0.00	0.16	0.00	0.00	0.51
SA 15	bdl	bdl	100.0	Po-Cb	45.65	51.29	0.00	0.10	0.00	2.96	0.00	0.00	0.47
PA 15	bdl	bdl	100.0	Po	52.04	47.16	0.00	0.72	0.00	0.09	0.00	0.00	0.52
PA 15	bdl	bdl	100.0	Ni-Cu sulfide	32.05	47.07	0.00	18.85	0.00	2.02	0.00	0.00	0.41
PA 15	bdl	bdl	100.0	Cb-Cp	30.73	49.93	0.00	1.01	0.00	18.34	0.00	0.00	0.38
PA 15	bdl	bdl	100.0	Po-Cb	48.95	47.80	0.00	0.27	0.00	2.98	0.00	0.00	0.51
PA 15	bdl	bdl	100.0	Cb	37.85	43.69	0.00	0.21	0.00	18.25	0.00	0.00	0.46
PA 14	bdl	bdl	100.0	Po-Cb	51.87	46.03	0.00	0.30	0.00	1.80	0.00	0.00	0.53
PA 14	bdl	bdl	100.0	Cb	39.00	43.45	0.00	0.00	0.00	17.55	0.00	0.00	0.47
PA 14	bdl	bdl	100.0	Po	52.12	47.02	0.00	0.33	0.00	0.54	0.00	0.00	0.53
PA 14	bdl	bdl	100.0	Po-Cb	47.86	46.18	0.00	0.27	0.00	5.69	0.00	0.00	0.51

of the PA-20 lava sample, being about 1,100°C (Table 6). The two applied thermometers (Putirka et al., 2003; Neave and Putirka, 2017) give similar values (Table 6) that fall within their uncertainties (±45°C).

The composition of pyrrhotite allowed calculating the sulfur fugacity by using the equation of Toulmin and Barton (1964), which relates the composition of pyrrhotite to sulfur fugacity and temperature. The calculated log of sulfur fugacity is 1.24, assuming a temperature of 1,000°C (amphibole thermometer applied to hornblende-rich enclave and PA20 lava) and 1.74, assuming a temperature of 1,100°C (clinopyroxene thermometers applied to the lavas).

Discussion

Magmatic sulfide inclusions

Magmatic sulfide inclusions trapped in phenocrysts were found in rocks from all three phases of the Rincón-Portezuelo de las Ánimas suite and in all samples, except for two shoshonites of the late phase and the high K dacite of the early phase. They are particularly abundant in the latites of the late phase and in the crystal mush rock enclave of the early phase. As for the Cu content, they are Cu-rich sulfides and minor pyrrhotite in the early phase, pyrrhotite with sporadic Cu-rich exsolution structures in the intermediate phase, only pyrrhotite in the late phase (Tables 1, 2; Fig. 4). The general picture from these data indicates that sulfide saturation was a common process in the Rincón-Portezuelo de las Ánimas plumbing system when the magmas reached an intermediate stage of evolution. This probably occurred in relatively deep magma chambers: thermobarometric calculations indicate that magmas of Rincón-Portezuelo de las Ánimas were stored at pressures of 450 ± 150 MPa, corresponding to depths of about 16 ± 5.5 km (assuming a crustal density of 2.8 g/cm^3, Lucassen et al., 2001), and temperatures spanning from 1,050° to 1,100°C (lavas) and 950° to 1,000°C (hornblende enclave cumulate). The studied samples do not show evidence of shallow (<200 MPa) magmatic reservoirs. The oxygen fugacity calculated for the sulfide-saturated Rincón-Portezuelo de las Ánimas magmas is around ΔNNO + 0.5 (Table 6). At these oxygen fugacity values and physicochemical conditions of crystallization, a substantial part of sulfur in the silicate melt is present as S^{2-}, as deduced by the application of the model of Jugo et al. (2010), indicating a S^{6+}/S_{total} ratio of around 0.5 (Table 6).

Apparently, the average Cu content of sulfides decreases from the early to the late phase (Table 1). However, it cannot be excluded that Cu-rich sulfides are the first to form when

Table 4. Major and Trace Element Contents (ppm) of Sulfide Inclusions (types 1 and 2 MSIs) Analyzed by LA-ICPMS (also shown are analyses of reference material MASS-1, error %, and detection limits)

Analysis	Sulfide	Spot size (μm)	V	Mn	Fe	Co	Ni	Cu	Zn	As	Se	Mo
Type 1 sulfide inclusions												
aa_1	SA10-fS1	10	2.0	238	278,503	1,257	3,663	317,021	504	-	252.4	-
aa_2	SA10-fS2	10	56.7	1,233	367,280	1,386	5,361	190,382	793	2.3	117.7	-
aa_3	SA10-fS3	10	78.7	795	347,303	711	2,047	452,129	765	0.2	83.2	-
aa_4	SA10-fS4	10	19.4	1,491	346,805	1,327	1,657	307,666	709	2.6	195.7	0.43
aa_5	SA10-fS6	10	113.9	895	372,705	1,730	2,939	77,957	204	-	48.9	-
aa_6	SA10-fS7	10	96.0	1,265	343,400	882	2,161	255,764	709	2.6	395.9	-
aa_7	SA10-fS8	10	16.2	969	381,605	1,057	1,786	221,925	695	0.9	255.5	0.74
aa_9	SA10-fS9	10	4.5	1,882	339,903	659	2,180	478,376	520	-	369.6	0.43
aa_10	SA10-fS11	10	21.5	806	325,305	872	3,705	349,357	727	1.4	66.7	-
Type 2 sulfide inclusions												
aa_8	SA10-fS10	10	67.9	1,234	602,502	2,503	4,658	241	99	-	94.7	0.19
aa_11	SA10-fS12	10	30.3	615	642,525	1,955	2,141	2,803	12	2.0	60.6	3.29
aa_12	PA20-lS1	10	5.4	477	627,205	2,110	2,412	116	6	-	33.3	0.24
aa_13	PA20-lS2	10	94.6	1,875	635,304	2,223	2,331	182	273	2.4	-	0.42
aa_14	PA20-lS3	5	1,112	15,900	577,503	1,023	-	7,824	1,987	-	557.4	25.60
aa_15	PA20-lS4	8	35.2	836	640,807	2,210	2,267	110	56	-	-	-
aa_16	PA20-lS5	10	74.4	1,492	641,305	1,776	2,249	3,487	326	0.4	57.5	2.82
aa_17	PA20-lS6	8	13.2	1,669	622,004	1,973	1,826	4,076	370	3.9	-	0.18
aa_18	PA20-lS7	8	203.1	12,592	630,702	1,234	1,448	1,437	1,387	-	-	6.48
aa_19	PA20-lS9	8	17.1	669	609,303	1,730	2,535	5,968	599	2.9	-	1.19
aa_20	PA20-lS11	5	1.2	-	626,505	1,844	1,873	305	244	-	-	0.67
aa_21	PA20-lS12	5	-	-	626,505	1,828	2,039	532	22	-	117.4	5.44
Mean type 1 [9]			45.42	1,064	344,756	1,098	2,833	294,508	625	1.10	198	0.18
Min-max type 1			2.0-113.9	238-1,882	278,503-372,705	659-1,730	1,657-5,361	77,957-478,376	204-793	0.2-2.6	48.9-369.6	0.43-0.74
Mean type 2 in PA20 [10]			155.6	3,551	623,714	1795	1,898	2,404	527	0.96	76.5	4.30
Min-max type 2 in PA20			1.2-1,112	477-15,900	577,503-641,305	1,023-2,223	1,448-2,535	110-7,824	6-1,987	0.4-3.9	33.3-557.4	0.24-25.6
Mean type 2 in SA10 [2]			49.1	925	622,513	2,229	3,399	1,522	55.5	1.00	77.63	1.74
MASS-1 (n = 7)			63.1	380.1	156,000	98.8	118.2	134,545	350,368	64.9	53.2	61.0
Error (%)			2.3	28.6		26.2	21	5.3	28.2	4.3	5.8	4.2
Detection Limit			0.02	0.40	2.10	0.03	0.70	0.06	0.24	0.04	1.10	0.01

Table 4. (*Cont.*)

Analysis	Rh	Pd	Ag	Cd	Sn	Sb	Te	Pt	Au	Tl	Pb	Bi
Type 1 sulfide inclusions												
aa_1	2.08	0.13	3.05	11.19	9.47	0.66	31.24	0.16	-	0.12	315.33	28.92
aa_2	0.98	0.96	83.97	28.27	8.18	-	-	-	-	3.30	1,478	92.35
aa_3	2.65	0.28	18.76	43.16	15.48	-	9.67	-	-	3.81	1,775	43.94
aa_4	1.75	0.98	57.64	54.71	8.96	-	78.38	2.95	6.51	4.01	549.20	167.47
aa_5	0.42	-	1.87	1.63	5.10	-	1.46	0.86	-	0.23	2.59	0.23
aa_6	1.38	0.29	47.12	57.35	10.58	0.71	45.36	-	0.20	4.84	13,651	313.24
aa_7	1.28	0.25	5.04	35.49	8.59	0.56	36.25	-	0.13	4.34	74.90	2.17
aa_9	2.30	0.27	15.87	89.50	6.07	0.03	64.50	-	0.10	4.62	4819	262.07
aa_10	1.64	0.21	0.47	38.50	11.80	-	6.81	-	-	0.53	1065	5.01
Type 2 sulfide inclusions												
aa_8	-	0.10	1.39	-	-	-	-	-	0.11	-	3.44	-
aa_11	0.02	-	13.31	1.28	-	-	-	-	-	0.10	39.78	1.51
aa_12	-	0.17	1.93	0.60	0.34	-	-	-	0.20	-	1.62	-
aa_13	-	-	-	-	3.05	0.67	13.14	-	0.19	-	1.22	0.18
aa_14	0.20	0.83	2.04	-	25.89	6.02	-	-	7.85	-	11.09	2.22
aa_15	-	-	1.30	1.79	3.99	1.59	-	-	0.34	-	1.25	0.05
aa_16	0.02	0.09	6.41	3.55	4.06	-	-	-	0.15	1.79	6.15	0.33
aa_17	0.02	0.36	1.02	4.51	2.93	-	-	-	0.67	-	2.69	0.35
aa_18	-	-	4.15	10.91	1.53	-	-	-	0.53	-	4.36	-
aa_19	0.02	-	0.40	-	-	-	-	-	0.41	-	4.11	-
aa_20	-	-	1.67	2.97	-	2.96	12.83	-	-	-	1.32	-
aa_21	-	-	-	-	13.14	-	39.08	-	2.22	1.02	2.18	-
Mean type 1 [9]	1.61	0.37	25.98	39.98	9.36	0.22	34.21	0.44	0.77	2.87	2637	102
Min-max type 1	0.42-2.65	0.21-0.98	0.47-83.97	1.63-89.50	5.10-15.48	0.03-0.71	1.46-78.38	0.16-2.95	0.10-6.51	0.12-4.84	2.59-13651	0.23-313.3
Mean type 2 in PA20 [10]	0.03	0.15	1.89	2.43	5.49	1.12	6.51	-	1.26	0.28	3.60	0.31
Min-max type 2 in PA20	0.02-0.2	0.09-0.83	0.4-6.41	0.6-10.91	0.34-25.89	0.67-2.96	12.83-39.08	-	0.2-7.85	1.02-1.79	1.22-11.09	0.05-2.22
Mean type 2 in SA10 [2]	0.01	0.05	7.35	0.64	0.00	0.00	0.00	-	0.06	0.05	21.61	0.76
MASS-1 (n = 7)	0.69	0.61	66.9	71.7	54.9	54.9	15.1	61.5	47.2	64.1	76.0	70.0
Error (%)	4.5	14.4	5.5	8.4	4.5	4.5	5.3	6.3	8.1	5.1	6.2	4.8
Detection Limit	0.01	0.01	0.01	0.02	0.04	0.01	0.04	0.01	0.01	0.01	0.01	0.01

Notes: Trace element concentrations in sulfide inclusions; Fe used as internal standard (based on EDS values); all values reported in ppm; - = below detection limit

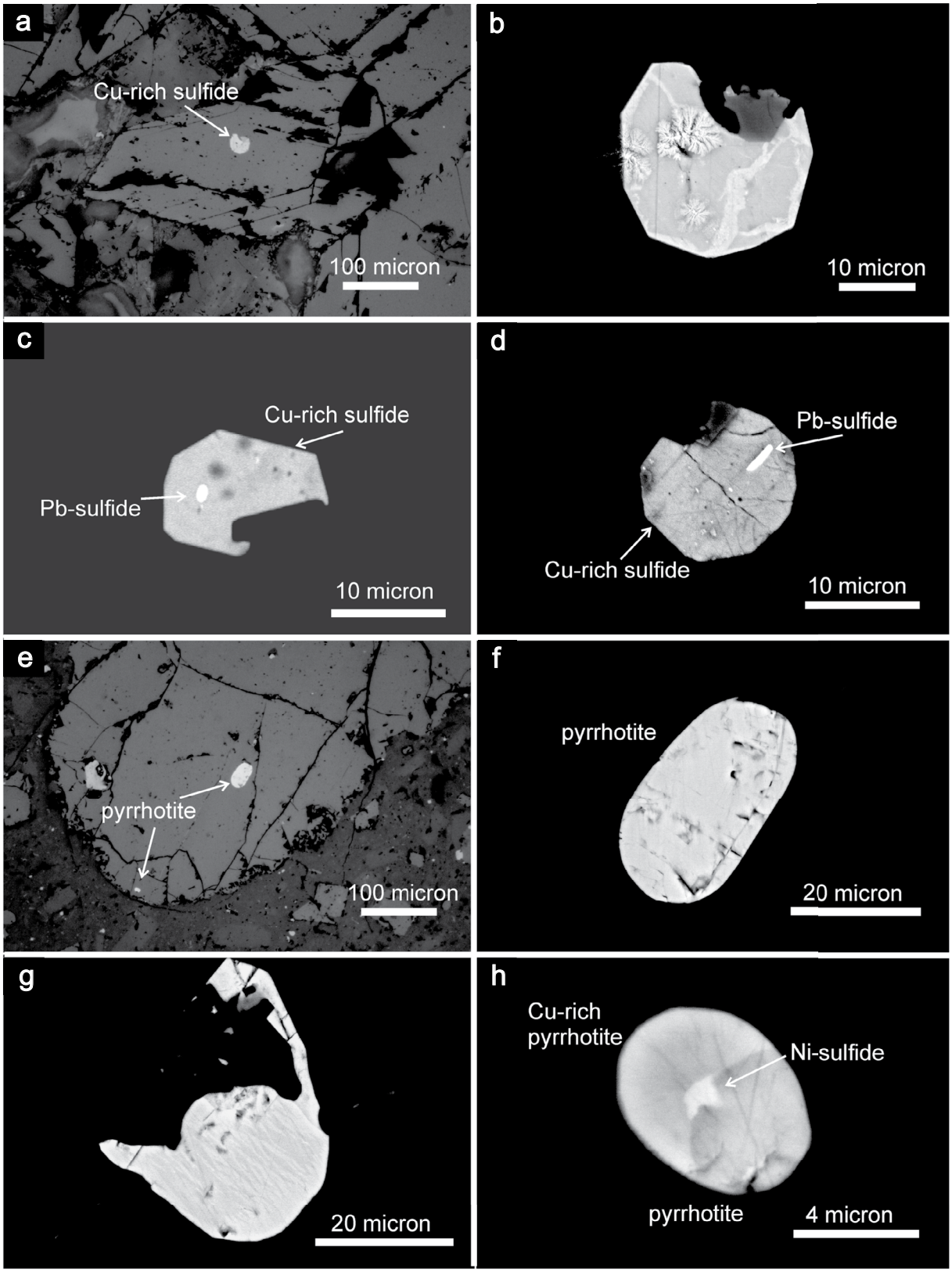

Fig. 4. a. Reflected light microphotograph of type 1 sulfide inclusion in hornblende. b. BSE image of unmixed type 1 sulfide inclusion (same as in (c)). c, d. BSE images of type 1 sulfide inclusions with unmixed Pb-rich sulfide phases. e. Reflected light microphotograph of type 2 sulfide inclusion in clinopyroxene. f. BSE image of type 2 sulfide inclusion (same as in (e)). g. BSE image of rare unmixed type 2 sulfide inclusion. h. BSE image of type 3 sulfide inclusions consisting of three different sulfide phases; the small bright one is Ni-rich sulfide.

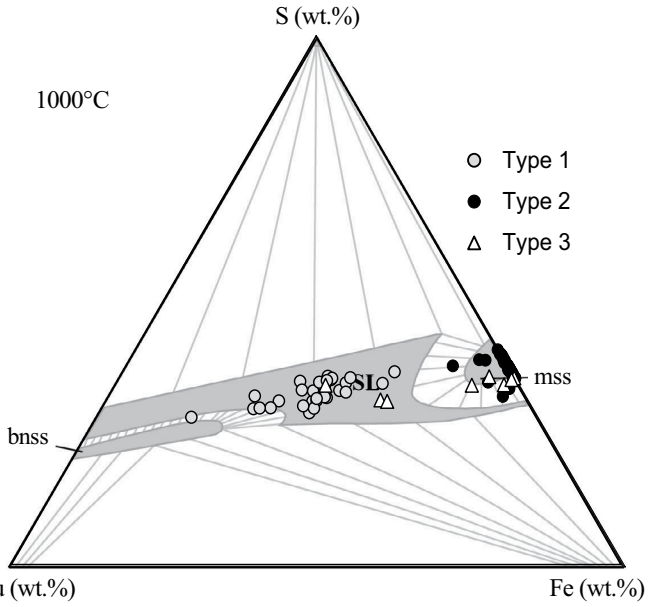

Fig. 5. Composition of sulfide inclusions in Rincón-Portezuelo de las Ánimas volcanic rocks, determined by means of EPMA and EDS (Table 2), plotted in the Cu-Fe-S system at 1,000°C (Craig and Kullerud, 1969). Unmixed inclusions (types 1 and 3), each dot corresponds to the analysis of a single sulfide phase in polymineralic inclusions.

saturation is achieved and thus, rather than being erupted with the lavas, they are stored in the crystal mushes in the crust and only by chance erupted, preferentially by explosive events. Within the intermediate phase, the Cu content of sulfides is higher in the least evolved andesites (Table 1), in agreement with a scenario of progressive copper depletion encountered by the silicate melt once sulfide saturation is achieved. No correlation between the MSIs and host mineral composition has been observed (Tables 3, 5). The paucity of sulfides in the groundmass of lavas as well as in the groundmass glass of the enclave may reflect, rather than the absence or scarcity of sulfides in the silicate melt, their syneruptive oxidation (Matsumoto and Nakamura, 2017) and/or their destabilization due to sulfur degassing (Edmonds and Mather, 2017, and references therein).

Magmatic sulfide inclusions could be trapped either as a liquid or as a solid, which can be either monosulfide solid solution (mss) or intermediate solid solution (iss), having a composition close to pyrrhotite and chalcopyrite, respectively (Parat et al., 2011). The nature of MSIs (liquid or solid) at the time of exsolution from magma and subsequent trapping is important because the partition coefficient between sulfide and silicate melt strongly depends on the nature of the sulfide phase (mss, iss, or sulfide liquid; Li and Audétat, 2015). Most of the observed MSIs have a rounded shape, however several recent papers indicate that the rounded shape of the sulfide phases cannot be used as an argument to justify their natures (liquid or solid, see Rottier et al., 2019, and references therein). If we report types 1 and 2 MSIs analyses on the ternary diagram of the Cu-Fe-S system at 1,000°C, the type 1 MSIs compositions fall in the liquid field, whereas type 2 MSIs fall in the pyrrhotite (mss) field suggesting that the latter were trapped as a solid phase. Indeed, the application of mineral geothermometers to Rincón-Portezuelo de las Ánimas products gave temperatures generally ≤1,100°C, which are consistent with the solidus temperature of monosulfide solid solution (Botcharnikov et al., 2013, and reference therein). Furthermore, the significant enrichment in Pb and Bi, and, to a lesser extent, Ag, observed in type 1 MSIs compared to the type 2 MSIs (Figs. 6, 7a-b, d), is consistent with the higher affinity of these metals to sulfide liquid compared to monosulfide solid solution. In fact, the log of partition coefficients sulfide liquid/silicate melt ($D_{SL/SM}$) and monosulfide solid solution/silicate melt ($D_{mss/SM}$) of Ag, Pb, and Bi varies from 3.14 ($D_{SL/SM}$) to 1.65 ($D_{mss/SM}$), 1.46 ($D_{SL/SM}$) to –0.90 ($D_{mss/SM}$), and 3.26 ($D_{SL/SM}$) to 0.69 ($D_{mss/SM}$), respectively. The partition coefficients are calculated for Rincón-Portezuelo de las Ánimas latitic magmas using bulk-rock analyses for silicate melt (App. 1) at 1,000°C, according to Li and Audétat (2015). The high Pb and Ag partitioning in the type 1 sulfides is emphasized by the Pb- and Ag-rich sulfide globules observed within several of them, representing, to our knowledge, the first finding of this type of unmixed phases in magmatic sulfides. The high correlation between Pb and Bi (Fig. 7d) emphasizes the analogous behavior of these elements in MSIs. The liquid nature of the type 1 MSIs may be in agreement also with their larger size. The sulfide inclusions occurring in the crystal-rich enclave are more abundant and larger in size than those trapped in phenocrysts in the lavas, similarly to what found by Georgatou et al. (2018) for sulfides in Ecuador volcanoes. This could be tentatively explained with the possibility of coalescence (and consequent increase in size) of liquid phase sulfides, carried by the silicate melt migrating in the crystallizing mush.

Type 3 MSIs are polymineralic and consist of pyrrhotite and of a sulfide with composition between pyrrhotite and cubanite, and in rare cases a small Ni sulfide (Fig. 4h). These different sulfides formed after trapping of the inclusion as a homogeneous phase. Due to the scarcity of these sulfides (only four of them could be analyzed; Table 3), more data would be needed to assess if they were trapped as sulfide liquid or as intermediate solid solution.

Comparison with mineralized systems

The metal content of types 1 and 2 MSIs of Rincón-Portezuelo de las Ánimas is here compared with that found in well-preserved MSIs from igneous rocks associated with porphyry mineralization (Fig. 8). The comparison shows a general good match, suggesting that at Rincón-Portezuelo de las Ánimas the attainment of sulfide saturation during fractionation in mid-upper crustal reservoirs produces magmatic sulfide phases having a composition comparable with those found in several porphyry systems.

The PGE contents in magmatic sulfides measured so far in Quaternary Ecuadorian arc rocks indicate a rather large range (<1 up to >20 ppm Rh, Pd 0.2–43 ppm, Georgatou et al., 2018), which is still wider if considering the sulfides analyzed in magnesian basalts of Kamchatka arc (up to 300 ppm Pd and 115 ppm Pt, Tolbachik volcano, Zelenski et al., 2017). The Rincón-Portezuelo de las Ánimas sulfides have PGE contents in the lower range of subduction-related magmas, with Rh of 1.6 ppm and Pt of 1.3 ppm in type 1 and Rh of 0.1 ppm and Pt <detection limit in type 2 MSIs; Pd is 0.4 ppm in both types (Table 4). The average Au content of types 1 and

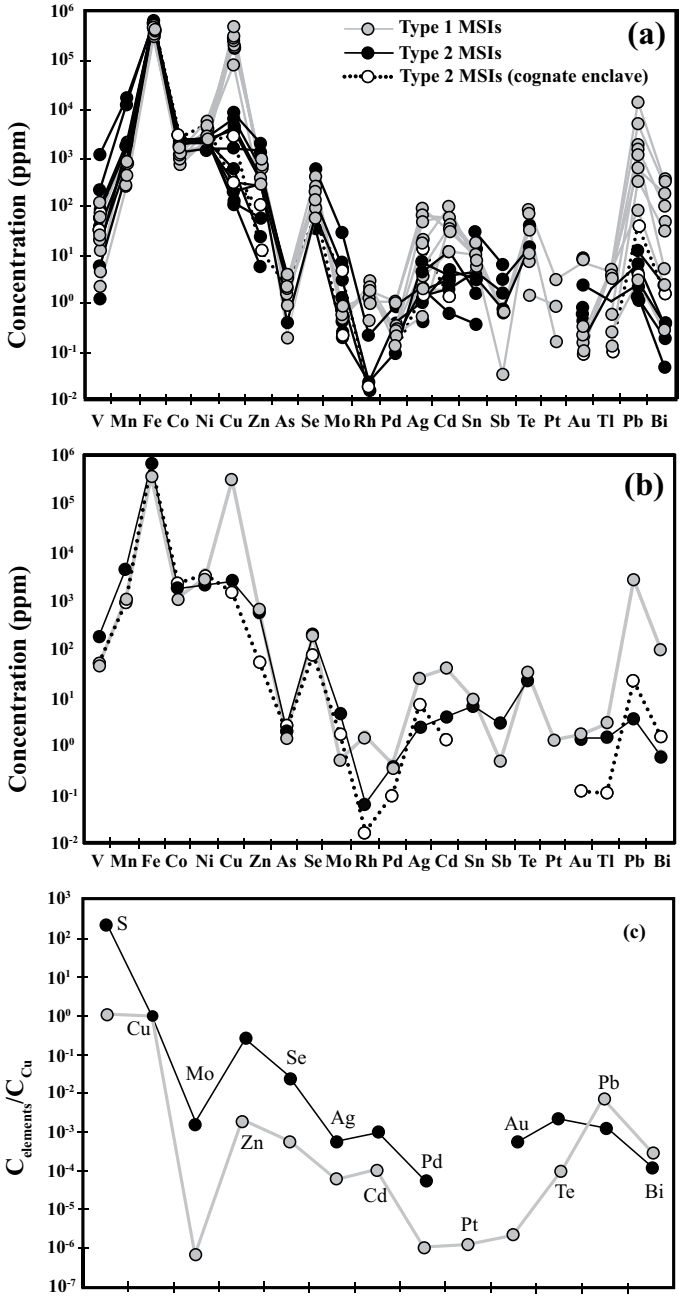

Fig. 6. Trace element composition of types 1 and 2 sulfide inclusions in Rincón-Portezuelo de las Ánimas volcanic rocks, measured by LA-ICPMS. Type 2 MSIs found in the cognate enclave with type 1 are distinguished. Absolute values of single inclusions (a), mean values for each type (b), and mean values of types 1 and 2 for selected elements normalized to Cu concentration (c).

2 MSIs is quite similar, although the Au concentration varies remarkably in both sulfide types (Fig. 8). These values fall in the range of average Au contents found in most MSIs from magmatic rocks associated with porphyry copper mineralization worldwide (Fig. 8; references in the figure key). Of particular relevance is the similarity between Au content of MSIs from the Rincón-Portezuelo de las Ánimas Volcanic Complex (both SL and mss) and the nearby and coeval Farallón Negro Volcanic Complex (mss, data from Halter et al., 2005), which is associated with the world-class Bajo de la Alumbrera porphyry copper deposit (avg Au content in Rincón-Portezuelo de las Ánimas type 1 MSIs = 0.8 ppm, in Rincón-Portezuelo de las Ánimas type 2 MSIs = 1.3 ppm, in Farallon Negro MSIs = 1.1 ppm). Furthermore, the average Au/Cu ratio of type 2 MSIs, which are sulfide inclusions of the same type (mss) based on the copper content, is about one order of magnitude higher than that calculated for MSIs of Farallón Negro (5.2×10^{-4} against 7.9×10^{-5}). These results strengthen the metallogenic potential of magmas generated in this back-arc sector of the Central Andes orogen. It is a matter of fact that, to our knowledge, no hydrothermal evidence for the presence of mineralization at depth has been reported in the outcropping Rincón-Portezuelo de las Ánimas volcanic deposits and basement rocks, although the economic potential at Rincón-Portezuelo de las Ánimas magmatic complex may be concealed by the low degree of erosion. The development of mineralization could be hindered by inappropriate local conditions for the development of a porphyry-style system, such as the lack of a shallow apophysis (at 2–5 km) focusing the metal-rich aqueous fluids exsolved by the magmatic system (estimated at around 11–20 km of depth according to the calculated pressure in Table 6). Other unfavorable factors may be excessive volcanic/intrusive ratios dispersing the volatile budget, insufficient amounts of mafic magmas feeding the crustal reservoirs and their size and duration of the mineralizing processes (Sillitoe, 2010). Moreover, the intermediate-evolved magmas at Rincón-Portezuelo de las Ánimas (evolved latites/high K dacites) were probably depauperated in Cu due to sulfide fractionation in intermediate magmas (Table 1). Noteworthy, the occurrence of hornblende-rich enclaves, representing the crystal mush at the wall of a deep (16 ± 5.5 km of depth) magmatic reservoir, which are enriched in Cu, Ag, Pb, Bi-bearing type 1 MSIs, may have a negative influence on the mineralization potential of the residual magma, analogous to the findings of Chang and Audétat (2018). However, these crystal mushes might represent an important preconcentration site where metals are stored inside and can be subsequently remobilized by remelting of these crystal mushes (Wilkinson, 2013). Our results underline that this may be relevant not only for Cu and precious metals but also for elements such as Pb and Bi, and to a lesser extent Ag and Cd, that strongly partition into a sulfide liquid.

Tectonomagmatic setting implications for magma fertility

Some considerations on metallogenesis in the slab-shallowing region at 27°S can be made in context of the tectonomagmatic setting in which the Rincón-Portezuelo de las Ánimas magmatic complex developed. The Rincón-Portezuelo de las Ánimas magmas have a strong subduction-fluid imprint and a hydrous nature, indicated by the abundance of hornblende and by the high Ba/Nb ratios of the Rincón-Portezuelo de las Ánimas volcanic rocks (up to 100, Gioncada, unpub. data; Vezzoli et al., 2011). This suggests that arc-type magmas can be generated by slab dehydration at this distance (presently over 500 km) from the trench. The geochemical features of Rincón-Portezuelo de las Ánimas (i.e., Sr/Y in agreement with normal arc, Gioncada, unpub. data) indicate that the crust was not thickened enough to induce the formation of magmas with adakitic features. The potassic (shoshonitic) affinity

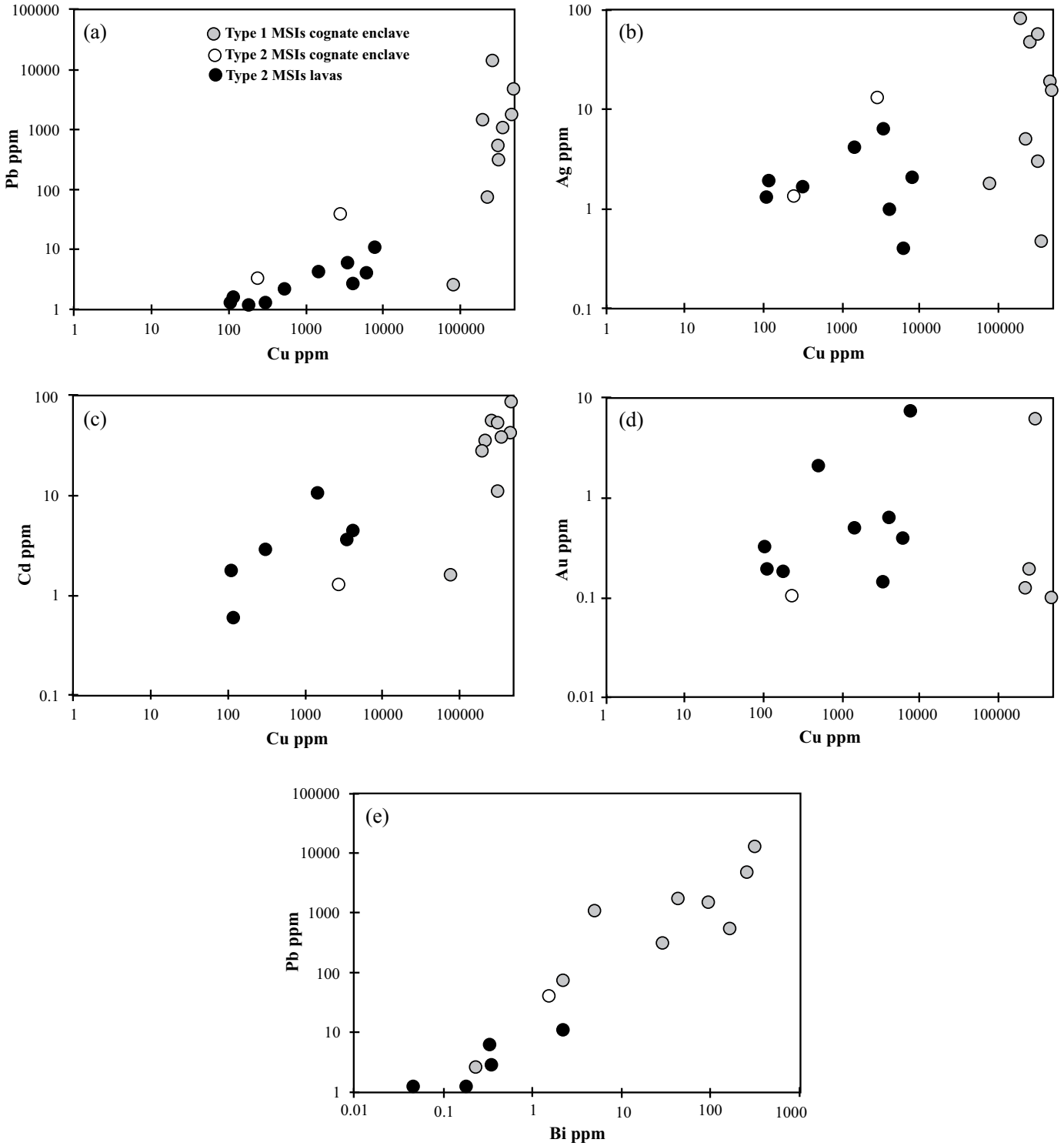

Fig. 7. Variation diagrams of Pb, Ag, Cd, and Au vs. Cu (a. b, c, d) and Pb vs. Bi (e) determined in types 1 and 2 MSIs.

of Rincón-Portezuelo de las Ánimas magmas increases from the early to the late phase (Fig. 2). The metal endowment, suggested by the metal content of sulfide inclusions and their high Au/Cu ratio, particularly for monosulfide solid solutions (Fig. 6c), may be a characteristic of the magma sources at this latitude. This is in agreement with the Cu-Au metallogenic domains recognized in this sector of Central Andes (Sasso and Clark, 1998).

The average and the range of Au content of types 1 and 2 MSIs found in Rincón-Portezuelo de las Ánimas rocks are substantially the same, despite the significant differences of gold partition coefficients between sulfide liquid-silicate melt

Table 5. Composition of Minerals Hosting Sulfide Inclusions (analyzed by EPMA)

Sample and host Sulfide	SA10-1 s1	SA10-2 s2	SA10-3 s3	SA10-4 s4	SA10-5 s5	SA10-6 s6	SA10-7 s7	SA10-8 s8	SA10-9 s19	SA10-10 s20	SA10-11 s21	PA20-5 s13
Amphibole												
SiO_2	40.77	40.63	40.05	40.87	40.24	40.94	40.50	39.57	40.36	40.04	40.48	39.84
TiO_2	2.36	2.53	2.56	2.40	2.48	2.54	2.74	2.43	2.39	2.36	2.46	2.45
Al_2O_3	13.48	12.83	13.16	13.01	13.13	12.86	12.77	13.40	13.07	12.99	13.01	13.10
FeO_t	13.21	11.80	12.70	12.03	12.37	12.44	12.46	12.45	12.30	12.61	11.93	13.63
MnO	0.20	0.11	0.15	0.10	0.20	0.22	0.17	0.22	0.09	0.17	0.14	0.23
MgO	12.75	13.74	12.81	13.72	12.81	13.73	13.20	13.45	13.73	13.36	13.61	12.79
CaO	11.96	11.69	11.76	12.01	11.96	11.73	11.78	12.05	12.03	11.95	11.98	11.33
Na_2O	2.03	2.04	2.00	1.99	2.05	2.05	1.99	2.02	2.14	2.01	1.99	1.74
K_2O	1.58	1.40	1.58	1.54	1.53	1.57	1.55	1.53	1.63	1.55	1.55	1.67
Formula on the basis of 24 (O, OH, F)												
Si	6.05	6.09	6.04	6.08	6.06	6.07	6.07	5.95	6.02	6.02	6.05	6.03
Al IV	1.95	1.91	1.96	1.92	1.94	1.93	1.93	2.05	1.98	1.98	1.95	1.97
Al VI	0.41	0.35	0.38	0.36	0.39	0.32	0.33	0.33	0.32	0.33	0.35	0.36
Ti	0.26	0.28	0.29	0.27	0.28	0.28	0.31	0.27	0.27	0.27	0.28	0.28
Fe^{2+}	1.64	1.48	1.60	1.50	1.56	1.54	1.56	1.57	1.53	1.59	1.49	1.72
Mn	0.03	0.01	0.02	0.01	0.03	0.03	0.02	0.03	0.01	0.02	0.02	0.03
Mg	2.82	3.07	2.88	3.04	2.87	3.03	2.95	3.01	3.05	2.99	3.03	2.88
Ca	1.90	1.88	1.90	1.91	1.93	1.86	1.89	1.94	1.92	1.93	1.92	1.84
Na	0.58	0.59	0.58	0.57	0.60	0.59	0.58	0.59	0.62	0.59	0.58	0.51
K	0.30	0.27	0.30	0.29	0.29	0.30	0.30	0.29	0.31	0.30	0.30	0.32
Mg/ $(Mg+Fe_t)$	0.63	0.67	0.64	0.67	0.65	0.66	0.65	0.66	0.67	0.65	0.67	0.63

Sample and analysis Sulfide	PA 20-1 s9	PA 20-2 s10	PA 20-3 s11	PA 20-4 s12	PA14-1 s14	PA14-3 s16	PA14-4 s17	PA14-5 s18	PA14-2 s15
Clinopyroxene									Orthopyroxene
SiO_2	51.56	49.72	51.73	49.51	51.96	51.45	51.10	50.74	51.75
TiO_2	0.27	0.48	0.30	0.47	0.37	0.61	0.30	0.31	0.11
Al_2O_3	2.25	4.58	2.40	4.02	2.78	3.47	2.71	2.13	3.03
FeO_t	8.71	10.51	7.21	9.90	7.95	8.57	8.28	9.54	21.25
MnO	0.28	0.35	0.20	0.29	0.23	0.26	0.43	0.54	0.66
MgO	15.72	13.93	16.64	13.87	15.19	15.04	14.41	14.30	23.08
CaO	20.54	20.09	20.28	20.49	21.19	20.25	21.62	21.04	1.27
Na_2O	0.25	0.41	0.29	0.29	0.29	0.31	0.24	0.33	0.02
K_2O	0.01	bdl	bdl	bdl	bdl	bdl	bdl	0.01	bdl
Cr_2O_3	0.11	bdl	0.23	bdl	0.05	0.04	bdl	bdl	0.06
Total	99.70	100.07	99.28	98.84	100.01	100.00	99.09	98.94	101.23
Formula on the basis of 6 oxygens									
Si	1.91	1.85	1.91	1.86	1.92	1.90	1.91	1.91	1.89
Al IV	0.09	0.15	0.09	0.14	0.08	0.10	0.09	0.09	0.11
Al VI	0.01	0.05	0.02	0.04	0.04	0.05	0.03	0.00	0.02
Ti	0.01	0.01	0.01	0.01	0.01	0.02	0.01	0.01	0.00
Fe^{3+}	0.08	0.11	0.07	0.09	0.04	0.03	0.06	0.10	0.09
Fe^{2+}	0.19	0.22	0.15	0.22	0.21	0.24	0.20	0.20	0.56
Mn	0.01	0.01	0.01	0.01	0.01	0.01	0.01	0.02	0.02
Mg	0.87	0.77	0.92	0.78	0.84	0.83	0.80	0.80	1.26
Ca	0.82	0.80	0.80	0.83	0.84	0.80	0.87	0.85	0.05
Na	0.02	0.03	0.02	0.02	0.02	0.02	0.02	0.02	0.00
K	0.00	0.00	0.00	0.00	0.00	0.00	0.00	0.00	0.00
Cr	0.00	0.00	0.01	0.00	0.00	0.00	0.00	0.00	0.00
Wo	41.74	42.14	41.33	43.12	43.66	42.30	44.92	43.48	2.54
En	44.45	40.66	47.20	40.62	43.55	43.72	41.66	41.13	64.27
Fs	13.81	17.21	11.47	16.26	12.79	13.97	13.43	15.39	33.19
Mg/ $(Mg+Fe_t)$	0.76	0.70	0.80	0.71	0.77	0.76	0.76	0.73	0.66

Table 6. Summary of the Results of Oxybarometry and Thermobarometry Calculations

Sample no.	T (°C)[1]	T (°C)[2]	T (°C)[3]	T (°C)[4]	P (MPa)[2]	P (MPa)[3]	P (MPa)[4]	$\log f_{S_2}$ (bar)[5]	ΔNNO[2]	$\log f_{O_2}$ (bar)	S^{6+}/S_{tot}[6]
SA-10	953–974	997–1025			462–547				0.4–0.7	–9.1/–9.7	0.33–0.67
PA-14			1077–1108	1112–1130		240–440	400–530	1.24–1.74			
PA-20	958	996	1086–1120	1104–1130	515	300–630	360–630	1.24–1.74	0.6	–9.6	0.57

[1] Putirka (2016); [2] Ridolfi et al. (2010); [3] Neave and Putirka (2017); [4] Putirka et al. (2003); [5] Toulmin and Barton (1964); [6] Jugo et al. (2010)

and monosulfide solid solution-silicate melt ($D_{SL/SM}$ ~10^4 and $D_{MSS/SM}$ ~10^2, calculated according to Li and Audétat, 2015; Figs. 6c, 7d, 8). This may suggest a different Au content of the magmas (with high K calc-alkaline/shoshonitic affinity) from which these sulfides exsolved. Mechanisms that could have contributed to subtract Au from the early phase magma include a previous separation of an Au-bearing sulfide liquid, or of an S-bearing fluid phase in which Au is preferentially partitioned in agreement with the findings of Zajacz et al. (2012). Alternatively, these differences may be reconducted to the magma sources, changing from high K calc-alkaline to shoshonitic affinity. Following Li and Audétat (2013), different P-T conditions in the source region stabilize either monosulfide solid solution or sulfide liquid, thus affecting the capability of sulfides to sequester Au and, consequently, the Au content of the primary silicate melts. These considerations may be of help when looking for explanations for the genesis of Cu-Au-bearing magmatic-hydrothermal ore deposits in back-arc regions with shoshonitic magmatism.

Conclusions

The Rincón-Portezuelo de las Ánimas magmas were stored in reservoirs at a depth of about 16 ± 5.5 km, at temperatures from 1,100° to 950°C, with an oxygen fugacity about ΔNNO + 0.5 and $\log f_{S_2}$ between 1.24 and 1.74 bars. Sulfide saturation was a common process in the plumbing system, occurring at an intermediate stage of evolution (high K basaltic andesite-latite). The Cu content of sulfides was highest at the onset of sulfide formation and decreased with magma evolution. Thus, at Rincón-Portezuelo de las Ánimas and similar magmatic systems, high amounts of Cu and other metals are likely stored in crystal mushes in deep magma chambers; therefore, the fertility of magmas that intrude the upper crust is strongly affected by the possibility that the metal-rich sulfide-bearing crystal mushes are included in the intrusion. The sulfides stored in the crystal mushes formed from a sulfide liquid phase that separated from the silicate melt, and, in agreement with the sulfide liquid/silicate melt partition coefficients, are particularly rich in Pb, Ag, Bi, and show immiscible Pb- and Ag-rich phases. We speculate that this may represent the potential source for hydrothermal Cu-Pb-Ag sulfide mineralization. Gold behavior seems instead to be controlled by additional mechanisms, linked to the shoshonitic magma source or to an early partitioning into an S-bearing fluid phase, besides sulfide-silicate melt immiscibility.

The concentrations of metals in Rincón-Portezuelo de las Ánimas sulfide inclusions are comparable to those found in magmatic rocks associated with porphyry systems. The Au content of magmatic sulfides of Rincón-Portezuelo de las Ánimas volcanic rocks is similar to that measured in sulfide inclusions of the same type (mss) in Farallón Negro, whereas the average Au/Cu ratio is higher. The absence of mineralization evidence at Rincón-Portezuelo de las Ánimas can be due to local factors, such as deep magma storage that was not suitable for exsolution of a metal-rich aqueous fluid, excessive volcanic/intrusive ratio that dispersed the volatile budget, size and duration of the magmatic activity, and possibly lack of mineralizing processes. Our results provide further data to understand the genesis of Cu-Au-rich magmatic-hydrothermal ore deposits in this sector of the Central Andes.

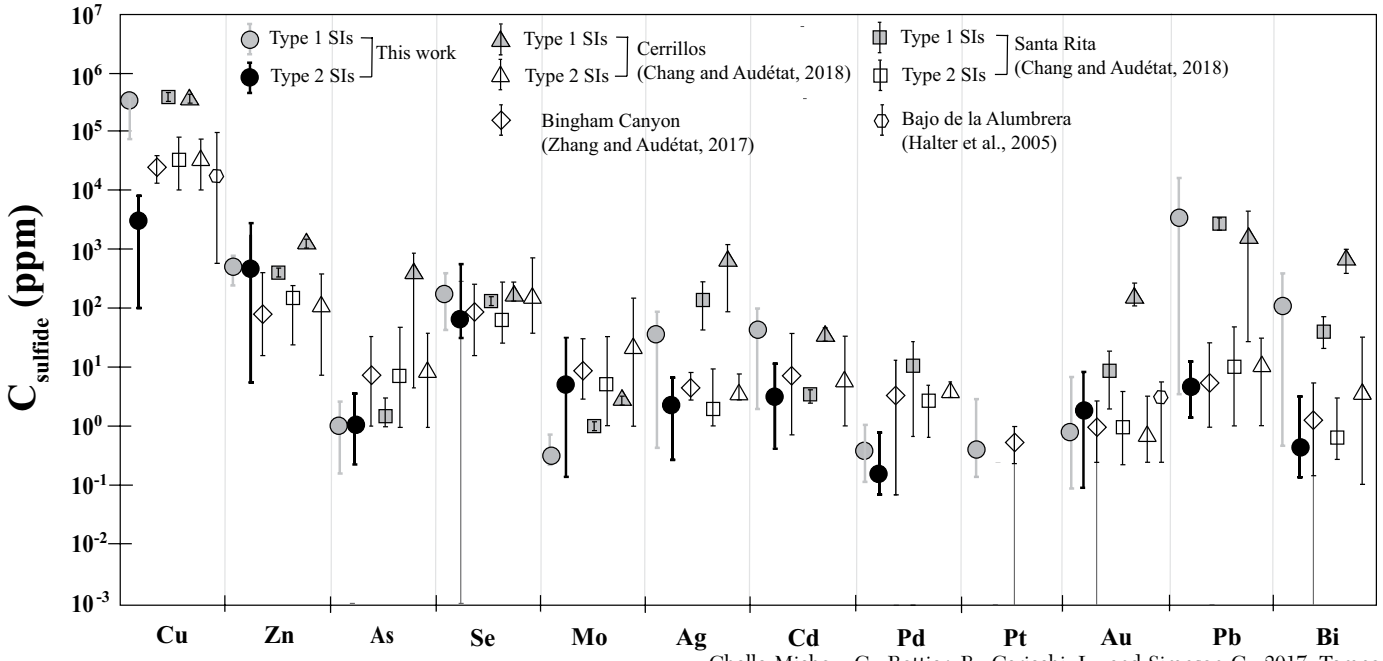

Fig. 8. Concentrations of metals (mean and range) in magmatic sulfides of Rincón-Portezuelo de las Ánimas compared to concentrations in magmatic sulfides in rocks related to porphyry copper deposits, available in the literature (Halter et al., 2005; Zhang and Audétat, 2017; Chang and Audétat, 2018; Rottier et al., 2019).

Chelle-Michou, C., Rottier, B., Caricchi, L., and Simpson G., 2017, Tempo

Acknowledgments

The authors are grateful to L. Folco and the Electron Microscopy Lab of the CISUP-University of Pisa and G. Poli and A. Risplendente of the Electron Microprobe Lab of University of Milan for their commitment to continuing their laboratory operations during the Covid-19 emergency, and assistance in collecting part of the data in this study. We also thank the students D. Mandalari and M. Raimondi for contributing to data collection. This paper benefited from reviews by Jeff Hedenquist and two anonymous reviewers, whose useful comments and suggestions helped to improve the quality and the clarity of the manuscript, for which we are thankful. This contribution is dedicated to the memory of Ricardo Héctor Omarini, whose love for Argentinian geology allowed all this.

REFERENCES

Audétat, A., and Simon, A.C., 2012, Magmatic controls on porphyry copper genesis: Society of Economic Geologists Special Publication 16, p. 1–18.

Bai, Z.-J., Zhong, H., Hu, R.-Z., and Zhu, W.-G., 2020, Early sulfide saturation in arc volcanic rocks of southeast China: Implications for the formation of co-magmatic porphyry-epithermal Cu-Au deposits: Geochimica et Cosmochimica Acta, v. 280, p. 66–84.

Botcharnikov, R.E., Holtz, F., Mungall, J.E., Beermann, O., Linnen, R.L., and Garbe-Schonberg, D., 2013. Behavior of gold in a magma at sulfide-sulfate transition: Revisited: American Mineralogist, v. 98, p. 1459–1464.

Cahill, T.A., and Isacks, B.L., 1992, Seismicity and shape of the subducted Nazca plate: Journal of Geophysical Research, v. 97, p. 17,503–17,529.

Carrasquero, S.I., Rubinstein, N.A., Gomez, A.L.R., Chiaradia, M., Fontignie, D., and Valencia, V.A., 2018, New insights into petrogenesis of Miocene magmatism associated with porphyry copper deposits of the Andean Pampean flat slab, Argentina: Geoscience Frontiers, v. 9, p. 1565–1576.

Chang, J., and Audétat, A., 2018, Petrogenesis and metal content of hornblende-rich xenoliths from two Laramide-age magma systems in southwestern USA: Insights into the metal budget of arc magmas: Journal of Petrology, v. 59, p. 1869–1898.

of magma degassing and the genesis of porphyry copper deposits: Scientific Reports, v. 7, p. 40566.

Chernicoff, C.J., Richards, J.P., and Zappettini, E.O., 2002, Crustal lineament control on magmatism and mineralization in northwestern Argentina: Geological, geophysical, and remote sensing evidence: Ore Geology Review, v. 21, p. 127–155.

Chiaradia, M., 2014, Copper enrichment in arc magmas controlled by overriding plate thickness: Nature Geoscience, v. 7, p. 43–46.

Chiaradia, M., and Caricchi, L., 2017, Stochastic modelling of deep magmatic controls on porphyry copper deposit endowment: Scientific Reports, v. 7, p. 44523.

Costa, S., Fulignati, P., Gioncada, A., Pistolesi, M., Bosch, D., and Bruguier, O., 2021, Tracking metal evolution in arc magmas: Insights from the active volcano of La Fossa, Italy: Lithos, v. 380–381, p. 105851.

Craig, J.R., and Kullerud, G., 1969, Phase relations in the Cu-Fe-Ni-S system and their application to magmatic ore deposits: Economic Geology Monograph 4, p. 344–358.

Edmonds, M., and Mather, T.A., 2017, Volcanic sulfides and outgassing: Elements, v. 13, p. 105–110.

Georgatou, A., and Chiaradia, M., 2020, Magmatic sulfides in high-potassium calc-alkaline to shoshonitic and alkaline rocks: Solid Earth, v. 11, p. 1–21.

Georgatou, A., Chiaradia, M., Rezeau, H., and Walle, M., 2018, Magmatic sulphides in Quaternary Ecuadorian arc magmas: Lithos, v. 296–299, p. 580–599.

González, O., Ortega-Rivera, A., and Zentilli, M., 2005, Geocronología del Complejo Volcánico Portezuelo de las Ánimas, Sierras del Aconquija, Provincias de Catamarca y Tucumán, Argentina: XVI Congreso Geológico Argentino, La Plata, Actas, v. 1, p. 777–782.

Halter, W.E., Pettke, T., and Heinrich, C.A., 2002, The origin of Cu/Au ratios in porphyry-type ore deposits: Science, v. 296, p. 1844–1846

Halter, W.E., Heinrich, C.A., and Pettke, T., 2005, Magma evolution and the formation of porphyry Cu-Au ore fluids: Evidence from silicate and sulfide melt inclusions: Mineralium Deposita, v. 39, p. 845–863.

Hao, H., Campbell, I.H., Richards, J.P., Nakamura, E., and Sakaguchi, C., 2019, Platinum-group element geochemistry of the Escondida igneous suites, northern Chile: Implications for ore formation: Journal of Petrology, v. 60, p. 487–524.

Jugo, P.J., Wilke, M., and Botcharnikov, R.E., 2010, Sulfur K-edge XANES analysis of natural and synthetic basaltic glasses: Implications for S

speciation and S content as function of oxygen fugacity: Geochimica et Cosmochimica Acta, v. 74, p. 5926–5938.
Kay, S.M., and Mpodozis, C., 2002, Magmatism as a probe to the Neogene shallowing of the Nazca plate beneath the modern Chilean flat-slab: Journal of South American Earth Sciences, v. 15, p. 39–57.
Kay, S.M., and Coira, B.L., 2009, Shallowing and steepening subduction zones, continental lithospheric loss, magmatism, and crustal flow under the Central Andean Altiplano-Puna Plateau: Geological Society of America Memoir 204, p. 229–259.
Kay, S.M., Mpodozis, C., and Coira, B., 1999, Magmatism, tectonism and mineral deposits of the Central Andes (22°–33°S): Society of Economic Geology Special Publication 7, p. 27–59.
Li, Y., and Audétat, A., 2013, Gold solubility and partitioning between sulfide liquid, monosulfide solid solution and hydrous mantle melts: Implications for the formation of Au-rich magmas and crust–mantle differentiation: Geochimica et Cosmochimica Acta, v. 118, p. 247–262.
——2015, Effects of temperature, silicate melt composition, and oxygen fugacity on the partitioning of V, Mn, Co, Ni, Cu, Zn, As, Mo, Ag, Sn, Sb, W, Au, Pb, and Bi between sulfide phases and silicate melt: Geochimica et Cosmochimica Acta, v. 162, p. 25–45.
Lucassen, F., Becchio, R., Harmon, R., Kasemann, S., Franz, G., Trumbull, R., Wilke, H.-G., Romer, R.L., and Dulski, P., 2001, Composition and density model of the continental crust at an active continental margin—the Central Andes between 21° and 27°S: Tectonophysics, v. 341, p. 195–223.
Matsumoto, K., and Nakamura, M., 2017, Syn-eruptive breakdown of pyrrhotite: A record of magma fragmentation, air entrainment, and oxidation: Contributions to Mineralogy and Petrology, v. 172, no. 10, p. 83.
Mc Innes, B.I.A., McBride, J.S., Evans, N.J., Lambert, D.D., and Andrew, A.A., 1999, Osmium isotope constraints on ore metal recycling in subduction zones: Science, v. 286, p. 512–516.
Middlemost, E.A.K., 1989, Iron oxidation ratios, norms and the classification of volcanic rocks: Chemical Geology, v. 77, p. 19–26.
Mungall, J.E., 2002, Roasting the mantle: Slab melting and the genesis of major Au and Au-rich Cu deposits: Geology, v. 30, p. 915–918.
Nadeau, O., Williams-Jones, A.E., and Stix, J., 2010, Sulphide magma as a source of metals in arc-related magmatic hydrothermal ore fluids: Nature Geoscience, v. 3, p. 501–505.
Neave, D.A., and Putirka, K.D., 2017, A new clinopyroxene-liquid barometer, and implications for magma storage pressures under Icelandic rift zones: American Mineralogist, v. 102, p. 777–794.
Parat, F., Holtz, F., and Streck, M.J., 2011, Sulfur-bearing magmatic accessory minerals: Reviews in Mineralogy and Geochemistry, v. 73, p. 285–314.
Park, J.-W., Campbell, I.H., Kim, J., and Moon, J.W., 2015, The role of late sulfide saturation in the formation of a Cu- and Au-rich mMagma: Insights from the platinum group element geochemistry of Niuatahi-Motutahi lavas, Tonga rear arc: Journal of Petrology, v. 56, p. 59–81.
Park, J.-W., Campbell, I.H., Malaviarachchi, S.P.K., Cocker, H., Hao, H., and Kay, S.M., 2019, Chalcophile element fertility and the formation of porphyry Cu ± Au deposits: Mineralium Deposita, v. 54, p. 657–670.
Peccerillo, A., and Taylor, S.R., 1976, Geochemistry of Eocene calc-alkaline volcanic rocks from the Kastamonu area, northern Turkey: Contribution to Mineralogy and Petrology, v. 58, p. 63–81.
Putirka, K.D., 2016, Amphibole thermometers and barometers for igneous systems and some implications for eruption mechanisms of felsic magmas at arc volcanoes: American Mineralogist, v. 101, p. 841–858.
Putirka, K.D., Mikaelian, H., Ryerson, F., and Shaw, H., 2003, New clinopyroxene-liquid thermobarometers for mafic, evolved, and volatile-bearing lava compositions, with applications to lavas from Tibet and the Snake River Plain, Idaho: American Mineralogist, v. 88, p. 1542–1554.
Ramos, V.A., and Folguera, A., 2009, Andean flat-slab subduction through time: Geological Society of London Special Publication 327, p. 31–54.
Richards, J.P., 2011, Magmatic to hydrothermal metal fluxes in convergent and collided margins: Ore Geology Reviews, v. 40, p. 1–26.
——2015, The oxidation state, and sulfur and Cu contents of arc magmas: Implications for metallogeny: Lithos, v. 233, p. 27–45.
Richards, J.P., and Kerrich, R., 2007, Special Paper: Adakite-like rocks: Their diverse origins and questionable role in metallogenesis: Economic Geology, v. 102, p. 537–576.
Richards, J.P., Jourdan, F., Creaser, R.A., Maldonado, G., and DuFrane, S.A., 2013, Geology, geochemistry, geochronology, and economic potential of Neogene volcanic rocks in the Laguna Pedernal and Salar de Aguas Calientes segments of the Archibarca lineament, northwest Argentina: Journal of Volcanology and Geothermal Research, v. 258, p. 47–73.
Ridolfi, F., Renzulli, A., and Puerini, M., 2010, Stability and chemical equilibrium of amphibole in calc-alkaline magmas: An overview, new thermobarometric formulations and application to subduction-related volcanoes: Contributions to Mineralogy and Petrology, v. 160, p. 45–66.
Rosenbaum, G., Giles, D., Saxon, M., Betts, P. G., Weinberg, R. F., and Duboz, C., 2005, Subduction of the Nazca Ridge and the Inca Plateau: Insights into the formation of ore deposits in Peru: Earth and Planetary Science Letters, v. 239, p. 18–32.
Rottier, B., Audétat, A., Kodera, P., and Lexa, J., 2019, Origin and evolution of magmas in the porphyry Au -mineralized Javorie volcano (Central Slovakia): Evidence from thermobarometry, melt inclusions, and sulfide inclusions: Journal of Petrology, v. 60, p. 2449–2482.
Sasso, A.M., and Clark, A.H., 1998, The Farallón Negro Group, northwest Argentina: Magmatic, hydrothermal, and tectonic evolution and implications for Cu-Au metallogeny in the Andean backarc: Society of Economic Geology Newsletter, no. 34, p. 6–18.
Sillitoe, R.H., 2010, Porphyry copper systems: Economic Geology, v. 105, p. 3–41.
Toulmin, P., and Barton, P.B., 1964, A thermodynamic study of pyrite and pyrrhotite: Geochimica et Cosmochimica Acta, v. 28, p. 641–671.
de Urreiztieta, M., Gapais, D., Le Corre, C., Cobbold, P.R., and Rossello, E., 1996, Cenozoic dextral transpression and basin development at the southern edge of the Puna Plateau, northwestern Argentina: Tectonophysics, v. 254, p. 17–39.
Vezzoli, L., Gioncada, A., Omarini, R., Guillou, H., Nonnotte, P., and Mazzuoli, R., 2011, The Miocene Rincon-Portezuelo de las Animas Miocene Volcanic Complex (sierras del Aconquija, Tucumán, Argentina): New geological and petrological data, *in* 1er Simposio Sobre Petrología Ígnea y Metalogénesis Asociada, San Miguel de Tucumán.
Wilkinson, J.J., 2013, Triggers for the formation of porphyry ore deposits in magmatic arcs: Nature Geoscience, v. 6, p. 917–925.
Yao, Z., and Mungall, J.E., 2020, Flotation mechanism of sulphide melt on vapour bubbles in partially molten magmatic systems: Earth and Planetary Science Letters, v. 542, p. 116298.
Zajacz, Z., Candela, P.A., Piccoli, P.M., Walle, M., and Sanchez-Valle, C., 2012, Gold and copper in volatile saturated mafic to intermediate magmas: Solubilities, partitioning, and implications for ore deposit formation: Geochimica et Cosmochimica Acta, v. 91, p. 140–159.
Zelenski, M., Kamenetsky, V.S., Mavrogenes, J.A., Danyushevsky, L.V., Matveev, D., and Gurenko, A.A., 2017, Platinum-group elements and gold in sulfide melts from modern arc basalt (Tolbachik volcano, Kamchatka): Lithos, v. 290–291, p. 172–188.
Zhang, D., and Audétat, A., 2017, What caused the formation of the Giant Bingham Canyon porphyry Cu-Mo-Au deposit? Insights from melt inclusions and magmatic sulfides: Economic Geology, v. 112, p. 221–244.

Paolo Fulignati received a Ph.D. degree in earth sciences from the University of Pisa in 1999. He has been working at Dipartimento di Scienze della Terra, University of Pisa, Italy, as a researcher since 2002, teaching Geochemistry Applied to Geothermics. His research interests have always been addressed to the petrology and geochemistry of "active" and "fossil" hydrothermal and magmatic-hydrothermal systems and the behavior of chalcophile elements in these environments, through a combination of field-based and mineralogical and geochemical methods (stable isotopes, trace elements, fluid and melt inclusion investigation).